Highlights

Deformation at the open-vent Erebus volcano, Antarctica, from more than 20 years of GNSS Observations

Ronni Grapenthin, Philip Kyle, Richard C. Aster, Mario Angarita, Terry Wilson, Julien Chaput

- Long-term Ross Island subsidence is consistent with Erebus edifice growth over the last 20 ka.
- Campaign and continuous GNSS data show years-long deformation transients attributed to volcano dynamics.
- Inflation-deflation cycles are modeled as pressure changes in the crustal and uppermost ($<\sim$1 km) magmatic conduit system.

Deformation at the open-vent Erebus volcano, Antarctica, from more than 20 years of GNSS Observations

Ronni Grapenthin[a], Philip Kyle[b], Richard C. Aster[c], Mario Angarita[a], Terry Wilson[d], Julien Chaput[e]

[a] *Geophysical Institute & Dept. Geosciences, University of Alaska Fairbanks, 2156 Koyukuk Drive, Fairbanks, 99775, AK, USA*
[b] *Dept. Earth Environmental Science, New Mexico Institute of Mining & Technology, 801 Leroy Pl., Socorro, 87801, NM, USA*
[c] *Department of Geosciences, Warner College of Natural Resources, Colorado State University, 1482 Campus Delivery, Fort Collins, 80523-1482, CO, USA*
[d] *School of Earth Sciences, Ohio State University, 125 South Oval Mall, Columbus, 43210, OH, USA*
[e] *Dept. of Earth, Environmental and Resource Sciences, University of Texas at El Paso, 500 W University, El Paso, 79902, TX, USA*

Abstract

Erebus volcano on Ross Island in Antarctica is an iconic open-vent volcano that has hosted a convecting anorthoclase-rich phonolite lava lake for at least 50 years. Recent magnetotelluric observations have imaged a conduit system originating at least 60 km below Erebus. This terminates in a seismically-imaged shallow magma reservoir about 500 m NW of the crater with an upper surface at about 500 m depth. A narrow and inclined terminal conduit system connects the shallow reservoir to the lava lake. Bomb-ejecting Strombolian eruptions from the lava lake and sporadically active adjacent vents are common. Larger eruptive activity with locally substantially elevated hazard has also been observed, including exceptionally energetic Strombolian activity in 1984 and an Inner Crater phreatic explosion in 1993. Despite sustained degassing and frequent eruptions, geochemical data show the composition of the lava has remained stable for the last 17 ka, consistent with the long-lived transcrustal magmatic system underlying the lake.

Global Navigation Satellite System (GNSS) data collection on Ross Island began in the late 1990s with campaign observations. In the early 2000s, additional benchmarks were added closer to the summit of Erebus and con-

Preprint submitted to Journal of Volcanology and Geothermal Research December 9, 2022

tinuous GNSS (cGNSS) sites were co-located with a seismic network. Today, seven cGNSS sites operate on the summit plateau and flanks of the volcano, and a network of eight campaign benchmarks has been surveyed episodically.

We present the first comprehensive geodetic data analysis and modeling results integrating these more than two decades of data collected at Erebus. We resolve long-term subsidence of Ross Island, which a simple viscoelastic model links to the long-term growth of Erebus over the last 20 ka. The data also show multi-year cycles of inflation and deflation in the summit area, consistent with activity in the shallow summit magmatic system. These small amplitude (several mm/yr) transient dynamics suggest multi-year pulses of pressurization and depressurization, or geometric changes within the shallow magmatic system that we can reproduce with analytical source models. The most recent inflation pulse lasted from November 2020 until March 2022 when several stations moved radially away from the shallow magmatic system and upwards at 10-15 mm/yr. Based on prior cycles, this deformation may result in increased eruptive active suggesting that continued and enhanced surveillance of Erebus is warranted. These observations contrast with the long-term general stability of the lava lake, but reflect Inner Crater dynamics, which can include changes in lava lake elevation and associated topographic changes of over 20 m on multi-year time scales. Our results emphasize the value of long-term and campaign-aided high-accuracy GNSS observations at open-vent volcanoes. This is especially true for volcanoes like Erebus which are remote and may only be accessible for a few months a year, and that deform at amplitudes and periods that may be difficult to resolve with satellite-based radar.

Keywords: Erebus, Antarctica, GNSS, volcano, deformation, magma system
PACS: 0000, 1111
2000 MSC: 0000, 1111

1. Introduction

Open-vent volcanoes provide a window into their underlying magmatic system that allows detailed investigation of magmatic processes driving their activity and behavior. Such systems are typically characterized by mild explosive activity and persistent gas emissions (Rose et al., 2013; Vergniolle and Métrich, 2021; Edmonds et al., 2022), making them an ideal place to develop and test monitoring techniques. However, open-vent volcanoes usually degas directly from their magmatic system. This prevents excessive pressure build up that would otherwise cause surface deformation of the volcano at magnitudes measurable with space-based remote sensing techniques such as interferometric synthetic aperture radar (InSAR) (e.g., Pritchard and Simons, 2002; Chaussard et al., 2013; Biggs and Pritchard, 2017) and Global Navigation Satellite System (GNSS, which includes the U.S. GPS) measurements (e.g., Shimada et al., 1990; Dzurisin, 2007; Grapenthin et al., 2013).

Erebus volcano on Ross Island in Antarctica (Fig. 1), hosts an active lava lake which has persisted for least 50 years following its discovery in 1973 (Giggenbach et al., 1973). First described by Sir James Ross in 1841 as "emitting smoke and flame in great profusion" (Giggenbach et al., 1973), Erebus continues its sustained degassing and persistent Strombolian eruptive activity to date (Aster, 2003; Dibble et al., 2008; Oppenheimer et al., 2011; Gerst et al., 2013). Long-lived active lava lakes are rare and are typically basaltic (e.g., Masaya, Erta 'Ale) or ultramafic (e.g., Nyiragongo), whereas the Erebus lava lake has a unique phonolitic composition (Kyle et al., 1992). Erebus phonolite magma has a high viscosity of 10^5-10^7 Pa s (Le Losq et al., 2015) when compared to the, e.g., 30 Pa s for the basalt in the lava lake at Erta 'Ale (Bouche et al., 2010; Lev et al., 2019). Typically kept open by continuous magma convection and degassing from depth, active lava lakes stand out among open-vent systems as the lakes form the top of the underlying magmatic system, allowing direct observations of magma system dynamics. Thus, these rare phenomena represent the ultimate observational window into an active magmatic system. Lev et al. (2019) present a global synthesis and review of the seven main global lava lakes in existence in 2018, three of which have since disappeared. The multidecadal lava lake at Erebus is thus exceptional, and its longevity may reflect a lack of shallow viscous stalling due to its low water content and high CO_2 flux (Hill et al., 2022).

Here, we examine over 20 years of campaign and continuous GNSS observations at Erebus volcano. We find geodetic evidence of both shallow magmatic dynamics and long-term subsidence of Ross Island, resolved over years-long time scales. This discovery emphasizes the need for longer duration ground- and satellite- based time series to resolve more subtle and lower signal-to-noise geodetic processes at active volcanoes that are commonly considered to be "non-deforming".

2. Background

2.1. Tectonics, Volcanic History and Activity

Volcanism in the western Ross Sea region is associated with extension of the West Antarctic Rift System (Behrendt, 1999; Jordan et al., 2020; Smellie et al., 2020), one of the largest continental rift zones on Earth. Ross Island sits at the south end of this province within the normal-faulting dominated Terror Rift, which is located in the Victoria Land Basin on the western edge of the larger rift system. Extension in the Terror Rift started about 17 Ma, but recent GNSS measurements indicate relative inactivity with insignificant spreading between East and West Antarctica (e.g., Donnellan and Luyendyk, 2004; Henrys et al., 2007; Fielding et al., 2008). Using teleseismic receiver functions Bannister et al. (2003) estimate a crustal thickness between 19–21 km under Ross Island, consistent with that previously suggested from seismic reflection data (e.g., Tréhu et al., 1993). Morin et al. (2010) additionally reported higher than average heat flow from the ANDRILL borehole AND-1B beneath the McMurdo Ice Shelf compared to the rest of the Victoria Basin.

Several processes affect deformation of Ross Island (Table 1). While the Terror Rift has been historically seismically quiet and exhibits little active extension, rebound in response to ongoing glacial unloading contributes perhaps 2 mm/yr of uplift (Willis, 2008). Thomas et al. (2011) suggest that Glacial Isostatic Adjustment (GIA) models overestimate the ongoing deformation caused by viscous mantle flux in Antarctica and careful correction of elastic rebound effects is required before GIA modeling. A currently unconstrained effect on vertical deformation is that of possible local sea-level drop due to reduced gravitational attraction arising from large-scale ice mass loss (Mitrovica et al., 2009). Since the Erebus summit plateau is ice free and not a substantial snow accumulation zone, and glaciers on the flanks or Erebus and at further distances on Ross Island are relatively stable as reflected in altimetry data that indicates near zero snow and ice mass change on and around Ross Island (Smith et al., 2020), we consider deformation due to local surface mass changes negligible. A perhaps surprising result by King and Santamaría-Gómez (2016) suggests that viscoelastic relaxation after the 1998 M_w 8.2 intraplate Balleny Islands earthquake offshore of East Antarctica measurably affected the deformation field around Ross Island. Depending on rheology, Ross Island may experience ≥1 mm/yr of horizontal response and ∼0.5 mm/yr of subsidence from this event. Another longstanding subsidence

Deformation Process	Expected Deformation	Reason to not consider	Relevant References
Rifting	≤1-2 mm/yr	low spreding rates, not well constrained	Donnellan and Luyendyk (e.g., 2004)
GIA	vertical 2 mm/yr (Willis, 2008)	large model errors, likely smoothly varying over Ross Island	Willis (2008); Thomas et al. (2011); Whitehouse et al. (2019)
local snow & ice mass change	near 0 mm/yr expected	no substantial snow and ice mass changes	Smith et al. (2020)
elastic and viscous response to potential local sea-level drop	?	unconstrained, ice history dependent	Mitrovica et al. (2009)
post-seismic response	≥1 mm/yr horizontal, ∼0.5 mm/yr subsidence	common to all sites, high uncertainty	King and Santamaría-Gómez (2016).
flexure due to Erebus loading	≥1-3 mm/yr	large model uncertainties	this paper

Table 1: Overview of non-volcanic deformation processes potentially affecting Erebus and Ross Island GNSS timeseries.

process relates to the formation of the flexural moat that surrounds Ross Island (Morin et al., 2010; Jha et al., 2022), likely induced by the island's loading of the thin, relatively warm crust. Subsidence due to volcanic loading has been suggested in other places (e.g., Hekla in Iceland, Grapenthin et al., 2010) and models show that this process can significantly affect a volcano's ability to transport magma to the surface; resulting in more evolved magmas or the cessation of eruptive activity altogether (e.g., Pinel and Jaupart, 2000).

Erebus, rising 3794 m above the Ross Sea, is the largest and only active volcanic center on Ross Island (Fig. 1; Martin et al. (2021); Sims et al. (2021)). The broad edifice forms much of the western part of Ross Island and is topped by an ~400 m high summit cone, which rises above a nearly circular 4 km-diameter summit plateau defined by multiple caldera rims. The lava lake is contained in the Inner Crater which is nested in the north end of the 600 m wide and 100 m deep Main Crater. The presence of the lava lake and its persistent eruptive activity shows no fundamental change over the last 50 years (Peters et al., 2014; Sweeney et al., 2008). This implies the continued presence of a shallow magma chamber and intact upper conduit system that feeds the lava lake. This magma chamber, in turn, requires long-term magmatic supply from a deeper source. Broad resolution magnetotelluric observations (Hill et al., 2022) show Erebus is underlain by a hot and continuous transcrustal magmatic system originating in the mantle over 60 km below Erebus. The deep conduit rarely generates internal volcanic or crustal seismicity (Rowe et al., 2000). Despite a paucity of internal seismic activity, the lava lake and associated vents in the Inner Crater are astonishingly dynamic. Some larger Strombolian eruptions from the lava lake can drop its level over ~3 m, which can refill within ~6 minutes (Aster et al., 2004; Dibble et al., 2008). Aster (2003) report that lava lake radii vary substantially over the years between 5-15 m, resulting in volume recharge between 235-2120 m^3 for 3 m lake level change. The Inner Crater floor and lava lake have shown significant morphological changes over the last 50 years. LiDAR and crater rim optical observations by Jones et al. (2015) document this dynamic system in detail for the period from 2008 to 2010, resolving aseismic lava lake level changes and crater floor elevation changes of ~3 m/yr, including net elevation reductions of the lava lake and adjacent Inner Crater features exceeding 20 m between 2001 and 2010. The shallow magmatic system feeding the lava lake was seismically imaged by Zandomeneghi et al. (2010) and Chaput et al. (2012). Zandomeneghi et al. (2013) interpreted a seismic velocity low and highly scattering body about 500 m NW of the lava lake with an upper surface near 500 m depth and underlying the high-temperature Tramways Ridge geothermal and microbial sector of the summit plateau (Noell et al., 2022) as a shallow lava lake linked magma body. Blondel et al. (2018) track this conduit system even deeper using scattering techniques that reveal a shallow inclined chimney-like structure connected to a magma reservoir at about 2.5 km bsl.

Sims et al. (2013) examined isotopic ratios from fresh lava bombs to show they had started degassing about 80 days prior to eruption. This indicates a significant resupply of magma and substantial gas flux and convective dynamics, which is substantiated by the observation of oscillatory zoning in the anorthoclase megacrysts that are ubiquitous in Erebus lavas and ejecta. Moussallam et al. (2014) interpreted crystal zonation as evidence for repeated bidirectional flow between the lake and a reservoir at a depth of up to several kilometers. Kelly et al. (2008) showed that the composition of the erupting lava has been similar over the last ∼17 ka. Long-term eruption rates estimated by Esser et al. (2004) show that Erebus has produced on average ∼4 km^3/ka over the last 250 ka, which is more than twice the 1.7 km^3/ka long-term eruption rate of the entire Erebus edifice when including activity older than 250 ka. Parmelee et al. (2015) used cosmogenic ^{3}He and ^{36}Cl exposure ages to date the 10 youngest lava flows on the summit plateau and these ranged from 4.5 to 8.5 ka. The average eruption rate over this period was estimated at 0.01 km^3/ka. Because the last major effusive activity was over 4 ka ago, the volcano is in a quiescent eruptive state.

2.2. History of deformation observations at Erebus

Some of the first geodetic observations on Erebus were performed from 1980–1985 during the International Mt. Erebus Seismic Studies (IMESS) project (Dibble et al., 1984). Blick et al. (1989) and Otway et al. (1994) report electronic distance and tilt measurements on the summit plateau and crater as well as within the Main Crater. All of their benchmarks have since been destroyed and cannot be remeasured, but they reported deformation on the order of 5±2 cm of extension across the 500 m-diameter Main Crater.

Geodetic observations utilizing the Global Navigation Satellite System (GNSS, specifically the U.S. Global Positioning System [GPS]) on Ross Island began in the mid-1990s with the installation of two sites at McMurdo Station (CRAR, MCM4; Fig. 1) and the establishment of other sites as part of the Transantarctic Mountains Deformation (TAMDEF) network. The TAMDEF campaigns focused on resolving deformation across the Transantarctic Mountains and the Terror Rift. They established three sites near the coast of Ross Island (Fig. 1, BIR0, ROY0, CRZ0) and one on the summit plateau of Erebus (ERE0). The Mount Erebus Volcano Observatory, assisted by UNAVCO, established eight additional campaign sites in the early 2000s: two on the slope of Erebus (HOOZ, SISZ), three on the summit plateau (EAST, HELZ, NAUS), and two on the crater rim (SHAC, RAYG). RAYG was destroyed by a lava bomb, and EUHT, a benchmark attached to Erebus Upper Hut, was lost when the hut was destroyed during a storm in October 2015. The entire campaign network (excluding CRZ0 in 2014/15) was remeasured during the 2014/15 and 2015/16 field seasons (Fig. 2).

Continuous GNSS observations began with single-frequency GPS, which we do not utilize in this work (these earliest data are available through UNAVCO, however). During the 2002–2004 field seasons the Integrated Surveillance Instrumentation network deployed a five-station broadband seismograph network with co-located dual frequency GPS (Aster et al., 2004). Of note was the modification of Guralp Systems CMG-DM24 seismic digitizers to enable recording and telemetry of continuous GPS phase and range observations in addition to broadband seismic data (Aster et al., 2004). As part of modernizing the geodetic network UNAVCO later replaced the GPS component of these systems with new polar mast installations supported by separate power systems. These sites are marked with a "2" in the four character station identifiers. In total, seven continuous GPS installations are currently (2022) operating on Erebus (Fig. 1, black circles); three on the flanks (ABBZ, HOG2, BOM2), three along the rim of the summit plateau (PHIG, CON2, MCG2), and NAU2 at Nausea Knob near the base of the active crater.

Figure 2 summarizes the available campaign and continuous GPS geodetic observations for Erebus and Ross Island collected over the past few decades. As each day with observations is marked by a dot, line segments indicate continuous observations. Interruptions reflect power outages or other technical failures in the challenging cold high-altitude Antarctic environment. These outages have been significantly reduced over the past decade due to advances in power systems and the dedicated engineering of the UNAVCO Polar Group (Hodge et al., 2018).

3. GNSS Data & Processing

We processed GNSS carrier phase and range observables into daily position time series for each station using NASA's Jet Propulsion Laboratory's (JPL) GipsyX 1.6 software (Bertiger et al., 2020) that implements precise point positioning (Zumberge et al., 1997) with ambiguity resolution, as applied to 24-hour data segments. Our solution strategy uses JPL orbit and clock products and International GNSS Service (IGS) antenna phase center models (Dow et al., 2009). Where available, we use JPL second-order ionospheric corrections, otherwise we fall back on those provided by the IGS. To correct tropospheric delays, we use the GPT2 model (Böhm et al., 2015) as implemented in GipsyX. Ocean tidal loading corrections utilize the TPXO7.2 and ATLAS model (Egbert and Erofeeva, 2002), a combination of hydrodynamic model and altimetric data with respect to Earth's center of mass (Fu et al., 2012) implemented in SPOTL (Agnew, 2012). We obtain position solutions for each station day in a fiducial-free reference frame, which we then transform into the 2014 International Reference Frame (ITRF14, Altamimi et al., 2016) using JPL transformation coefficients. We generate position time series relative to the stable Antarctic plate by removing the plate velocity model of Argus et al. (2010). Since we have no survey ties for any stations with newer monuments except NAUS, we connect the time series of old and new monuments by estimating a step offset between the average positions of the last observations at the old and the first observations at the new monument. Station velocities and uncertainties are inferred from the daily position time series, either as a whole or for time periods of interest, using Create and Analyse Time Series (CATS), version 3.1.1 Williams (2008). We solve for velocity, and for annual and semi-annual sinusoidal seasonal motions, assuming a power law noise model with flicker noise characteristics for continuous sites and white noise for campaign observations.

The transition from campaign to continuous observations resulted in obvious step artifacts in the vertical components at ABBZ, HOG2 and NAU2 (compare Fig. 3 and Fig. A.1). We presume that this reflects a reference point discrepancy between campaign (performed with levelling mount) and permanent installation, which cannot be corrected for NAUS and HOOZ as the monuments have been abandoned and is undocumented for ABBZ. Instead, we estimate an offset at the time of the transition using a Heaviside step function. Table 2 reports the estimated offsets for all three components. Working with the assumption that this is an antenna reference point issue, we correct only the vertical offset at the reported times. We consider that the horizontal components are not affected and any offsets are due to physical processes, which is justified when examining the full time series (Fig. 3). We suspect a similar issue at BOMZ, but do not attempt to correct this as the time between last campaign observation (2003-11-25) and first dual frequency continuous observation (2011-02-04) is more than seven years and any step correction estimation would be an overestimate.

4. Results

4.1. Long-term Velocities

We use the full time series for each campaign and continuous station to estimate the long-term velocities after removing the Antarctic Plate motion.

Station	Dec. Year	ΔN (mm)	σ_n (mm)	ΔE (mm)	σ_e (mm)	ΔV (mm)	σ_v (mm)
ABBZ	2004.095628	-1.6	0.4	-3.5	0.3	-35.7	1.2
HOOZ	2003.000000	0.4	0.4	-3.6	0.6	-25.7	1.6
NAUS	2003.000000	7.8	0.9	-0.6	0.5	-24.4	2.0
BOMZ	expected, not estimated: time between last campaign & first continuous too long						

Table 2: Offsets estimated at transition from campaign to continuous observations.

Figure 1 displays the plate velocity free horizontal and vertical velocities for Erebus and other Ross Island sites. The long-term horizontal velocities are generally small, up to ∼3 mm/yr, and almost zero outside the summit plateau of Erebus. At Cape Crozier, on the extreme east side of Ross Island, site CRZ0 is a notable exception. Much of the motion is due to a single repeat campaign in 2016. From 1997 until 2005/06 the horizontal velocities appear much smaller (Fig. A.11). When the Erebus summit plateau data are combined with sites on the flanks of the volcano (ABBZ, HOG2, SISZ) the small horizontal velocities appear to be somewhat systematically pointing toward the active vent. Some sites (ABBZ, BOM2, HOG2) appear to align with the plate velocity vector of 14.5 mm/yr shown in dark gray in Figure 1.

The vertical velocities across the network indicate subsidence. Although the coastal campaign sites suggest fairly uniform subsidence around 1 mm/yr, the continuous sites at McMurdo and Scott Base show slightly smaller subsidence of about 0.5 mm/yr. The uncertainties in these estimates are less than 0.05 mm/yr. Toward the summit of Erebus and the lava lake, the vertical velocities tend to increase at most stations as distance to the lava lake reduces. Notably, some sites such as ABBZ, BOM2, PHIG and CON2 show practically zero average vertical deformation rates over their lifetime.

4.2. Continuous GNSS Time Series

In Figure 3 (lower three panels) we assess the time history of the currently operational continuous GNSS sites after removal of the Antarctic Plate velocity. Several stations (ABBZ, HOOZ, BOMZ, NAUS) had campaign observations until about 2003 when continuous instrumentation was installed. Figure 3 has any discontinuities due to the change in observation strategy removed as detailed in Table 2. The non-adjusted time series are shown in Figure A.1. These long-term observations, spanning 1998 until 2022, particularly in combination with the early campaign observations, give a more dynamic picture than the average velocities shown in Figure 1 would suggest. In Figure 3, we identify four distinct episodes of Erebus-wide deformation. These episodes are especially obvious at NAUS/2 and CONG/2. In summary, from early 2000 until November 2004, motion was away from the lava lake, but changed to motion toward the vent from November 2004 to November 2011. No significant motion is obvious from November 2011 to October 2020, followed by renewed motion away from the lava lake between November 2020 and March 2022.

We observe weak pulsing behavior at some sites during these four episodes of deformation. Noticeably at CONG/2 the east component indicates a non-continuous process that shows similarities to observations at HOOZ. Data outages at NAUS/2 make it difficult to conclusively declare the period from 2011 – 2020 as quiescent, motions at CONG/2, PHIG, and MACG/2 suggest a short period of motion away from the edifice from about December 2016 until about June 2017, but at smaller magnitude than during other periods. Given this, the low radiative power (Fig. 3), and the lack of campaign observations spanning this period, we do not consider this period for more detailed analysis.

The estimated velocities for all available stations in the time intervals identified in Figure 3 are shown in Figures 4–6 and in Table 3. This confirms the general sense of motion we infer from Figure 3, but also provides spatial coherence with estimated uncertainties for the velocities.

Until November 2004 (Figure 4) we see consistent motion away from the lava lake for all stations on the summit plateau. This approaches 5 mm/yr in horizontal motion and is clearly above the noise. At the flank stations (ABBZ, HOOZ, BOMZ, and SISZ) this picture is not as clear, with SISZ showing coherence with the summit sites, but no discernible horizontal motion at the other locations. The vertical components show a complex picture of positive and negative velocities that do not clearly exceed uncertainties.

From November 2004 until November 2011 (Figure 5) the earlier motion reverses. All available station vectors point toward the lava lake and down. The uncertainties are much reduced due to the longer observation period of these continuous sites. The horizontal velocities first increase with distance away from the vent across the summit plateau to CONG and then decrease for stations on the flanks and beyond, but the trend is notable at ABBZ. The vertical velocities also decrease from NAUS with about 5 mm/yr the largest, CONG and MACG about 3 mm/yr to approximately 1 mm/yr with similar

Lon	**Lat**	**east**	**north**	**up**	σ_e	σ_n	σ_u	**site id**
		(mm/yr)						
pre-2004								
166.90895	-77.45688	-0.35	0.60	-1.96	0.69	0.72	3.14	ABBZ
166.39560	-77.27810	-0.21	-0.35	1.61	0.34	0.38	1.22	BIR0
167.44020	-77.50890	0.34	1.84	-3.93	0.50	0.45	1.83	BOMZ
167.08547	-77.53459	-2.83	-0.11	-5.58	1.11	1.19	4.08	CONG
169.33230	-77.51300	0.67	0.42	-0.83	0.18	0.10	0.33	CRZ0
167.22470	-77.51940	1.55	1.74	-0.51	0.48	0.63	1.49	EAST
167.15360	-77.51100	1.54	4.91	6.47	0.67	0.43	1.60	ERE0
167.17760	-77.50530	1.63	3.15	-5.17	0.60	0.41	2.24	HELZ
166.93263	-77.53160	-1.95	0.33	-5.38	0.89	0.93	2.97	HOOZ
166.66933	-77.83835	0.25	-0.27	2.42	0.42	0.41	1.36	MCM4
167.14714	-77.52196	0.23	3.68	0.82	0.85	0.81	2.89	NAUS
166.17062	-77.55157	0.65	0.40	-0.13	0.20	0.18	0.89	ROY0
166.97720	-77.56280	-1.83	-2.12	-4.36	0.34	0.47	1.24	SISZ
2004-2011								
166.90895	-77.45688	1.00	-1.70	-1.73	0.38	0.41	1.40	ABBZ
167.08547	-77.53459	3.62	0.94	-1.46	0.23	0.23	0.82	CONG
167.13955	-77.53038	0.69	0.87	-5.05	0.23	0.23	0.83	E1G2
166.93263	-77.53160	1.99	-0.42	-1.95	0.29	0.29	1.06	HOOZ
167.24664	-77.53255	-2.57	0.64	-1.96	0.43	0.42	1.61	MACG
167.14714	-77.52196	0.61	-4.05	-6.11	0.26	0.28	1.02	NAUS
2020-2022								
166.90895	-77.45688	-1.38	1.84	2.29	0.18	0.27	0.65	ABBZ
167.44024	-77.50894	2.32	-1.58	3.81	0.19	0.28	0.70	BOM2
167.08437	-77.53492	-6.50	-4.30	6.47	0.17	0.20	0.70	CON2
166.93362	-77.53145	-3.06	-0.39	2.48	0.21	0.22	0.82	HOG2
167.14677	-77.52185	-0.16	5.85	11.63	0.18	0.20	0.69	NAU2
167.04992	-77.52549	-6.23	-0.23	8.28	0.18	0.20	0.75	PHIG

Table 3: GNSS station locations, ids, velocity estimates and uncertainties during periods of deformation indicated by the time periods above table sections. Offsets identified in Table 2 were estimated simultaneously and thus do not affect the velocities.

uncertainties at ABBZ.

After a period of predominant quiescence from November 2011 until about October 2020, we detect an ongoing episode of motion away from the lava lake (Figure 6). The motion is opposite to that seen from 2004 until 2011. Horizontal motion is radially away from the lake and vertical motion is up. Notably, the rates of deformation during this shorter period are significantly larger than during any of the previous phases of deformation. Horizontal velocities are about 6 mm/yr at NAU2, PHIG, and CON2 and vertical velocities decrease from almost 12 mm/yr at NAU2 to 8 mm/yr at PHIG, and 6.5 mm/yr at CON2. On the flanks at ABBZ and HOG2 the motions are smaller, but still noticeable with somewhat surprising rates of vertical deformation of 2.5 mm/yr at HOG2 and 2.2 mm/yr at ABBZ.

5. Discussion

The decades-long geodetic observations on Ross Island and Erebus reveal two key observations: (1) apparent net subsidence of the island that appears to correlate with topography (Figure 1) and (2) multi-year transient deformation episodes observed at the continuous sites. Prior to interpreting these signals, it is important to acknowledge that they are small in magnitude, and occur in a region with multiple superimposed and opposing processes, including GIA uplift and flexural loading (Table 1). However, the signals, while small in amplitude, are convincingly associated with the volcano through their spatial and temporal coherence with respect to the vent and lava lake. While it is beyond the scope of this paper to exhaustively model and explain all contributions to the observed signals, we investigate first-order processes in an attempt to interpret principal observations.

5.1. Long-term Velocities

To investigate the source of the island-wide subsidence, we develop a load model to assess lithospheric viscoelastic response to the progressive growth of Erebus volcano. Esser et al. (2004) estimated characteristic long-term lava production at Erebus as 4 km^3 per 1000 years. We create a simple model distributing a 4 km^3 volume within a 250 m by 250 m grid of 3 km radius around the vent. This results in about 147 m of lava deposited every 1000 years. We model the lithospheric response as the surface displacement of an elastic plate with a Young's modulus of 80 GPa and a Poisson's ratio of 0.25

over a half space with a viscosity of 1x10^{19} Pa s (e.g., Ivins et al., 2022) using the software RELAX (Barbot and Fialko, 2010b,a).

Figure 7 shows the model predictions (blue) in comparison to observed long-term velocities. The predicted contemporary velocity pattern agrees well with the observations along the coastal sites of about 1 mm/yr of subsidence, with very small horizontal velocities pointing toward the load center (taken as the Erebus lava lake location). As expected, the vertical velocities increase toward the load center and reproduce the long term velocities at some summit plateau stations remarkably well (SHAC, E1G2, NAUS, ERE0, HELZ, EAST). However, this is not the case for summit plateau "rim" sites which show little to no long-term subsidence; as horizontal motion decreases toward the center of a surface load (e.g., Grapenthin, 2014) the observed long-term horizontal velocities are clearly not well reproduced by this model.

It is important to remember that these observations include a mix of campaign stations and varying observation times at continuous sites. PHIG, for instance, is a relatively new monument erected in 2013, but observations at the nearby site CONG/2 reach back almost 20 years. This certainly impacts the uncertainty estimates, but perhaps also the long-term velocities given the overall small rates. The Ross Island campaign sites were mostly observed annually in the early 2000s and then again in 2015 and 2016. This may result in the larger vertical velocities observed at BIR0, ROY0, and CRZ0 compared to the continuous sites SCTB and MCM4 near McMurdo.

Although the spatial dimensions of the simple load model are probably too small, we find it encouraging that this model reproduces the primary characteristics of the long-term vertical velocities increasing from shore toward the summit of Erebus. However, given the above caveats related to the data, the simplicity of the model, and the substantial range in deformation predictions from current GIA models (e.g., Whitehouse et al., 2019) that we have not considered here (albeit expected to be relatively constant across the small footprint of Ross Island), we refrain from further refinement of this model at this stage, but consider this a promising avenue for the future.

An alternative model to deformation driven by surface loading could be deflation of a deep magmatic source. While the aperture of the GNSS stations on Ross Island is small, we still would expect larger contributions to the horizontal components (Grapenthin et al., 2010). For instance, at 1 source depth radial distance from a pressure point source horizontal and vertical deformation is of approx. equal amplitude (e.g., Segall, 2010; Sigmundsson et al., 2018).

5.2. Time-varying Transient Deformation

Since the time-varying deformation patterns are spatially aligned with the shallow magmatic system, we interpret and model them to first order with classic analytical magma sources. This is justified by independent observations of volcanic activity shown in Fig. 3 (Top Panel) where MODIS-inferred radiant flux between 2000-2022 (Wright, 2016), here interpreted as correlated to lava lake size and activity, increases during the initial inflation period until November 2004 and remains at high levels until just prior to the end of the deflation period in November 2011. The seismicity between 2003-2011 analyzed by Knox et al. (2018) similarly correlates with the geodetically inferred activity showing few weekly eruptions during the inflation period followed by substantially higher numbers of weekly events during the beginning of the deflation period where one would expect higher volcanic activity. Since accessibility to Erebus is limited to the short period of the austral summer and because its volcanic hazard is relatively low, various existing data sets and studies beyond the ones shown in Fig. 3 are temporally sporadic.

Employing a bounded non-linear least squares inversion implemented in SciPy (Virtanen et al., 2020), we tested a range of analytical solutions that relate subsurface pressure changes to surface deformation including a pressure point source (Mogi, 1958), a general spheroid (Yang et al., 1988), and circular (Fialko and Simons, 2001) and rectangular (Okada, 1992) sill-like sources. All source models assume a homogeneous elastic half space, which is a common assumption in volcanic deformation modeling, albeit unquestionably simplistic (Masterlark, 2007). We test these sources for inflation during the time periods prior to November 2004 and from November 2020 until March 2022, and for deflation from November 2004 until November 2011. We present the best fitting solutions for each time interval. In this modeling, we weight the east, north and vertical residuals at each station by the reciprocal of the estimated velocity uncertainty.

Given the imperfect load model described above, and the generally lower long-term vertical and horizontal velocities, compared to the short-term transients (compare Figure 1 to Figures 4-6), we do not correct the short-term transient velocities for superimposed processes (GIA, Ross Island loading, post-seismic, see Table 1). This is justified as we expect the large uncertainties in the respective model corrections to introduce biases of similar or larger amplitude than these currently unmodeled signals (see, e.g., King et al., 2016, for GIA and plate velocity separation issues).

5.3. Inflation until November 2004

We employed various strategies to model the pre-2004 velocity field. The incoherent nature of the vertical velocities must be seen in the context of their large uncertainties (see Figures A.2–A.33; for instance CONG) and the almost identical subsidence signal of about 2–4 mm/yr at ABBZ, BOMZ, and SISZ. Given the latter, we omitted the non-plateau sites ABBZ, BOMZ, SISZ, and HOOZ from the determination of our preferred model. Figure 8 shows the predicted velocities for a dike (90° dip) striking about 120° from north with its centroid located between NAUS and the lava lake at about 2059 m asl. Its length and width are resolved as about 150 m and about 1 km, respectively, making it a thin and tall structure that opens about 0.32 m/yr during this time period (see Table 4). This model predicts velocities at the summit plateau sites well within the observed uncertainties. The horizontal velocities at ERE0, HELZ, NAUS, and EAST are almost exactly captured by this model.

Experiments that included the four sites on Erebus' flanks resulted in a similar model, pulled to the south and smaller length and width, and larger opening, but similar strike, dip and depth. Another modeling experiment in which we subtract the average subsidence at ABBZ, BOMZ, and SISZ from all vertical velocities also results in a similar model with changes to the dimensions and opening, but similar orientations.

To better assess how well the data constrain this model, we perform a Bayesian inversion using a Markov-Chain Monte-Carlo (e.g., Aster et al., 2018) approach for the dike-like geometry. Figure A.34 shows the posterior probability density functions for each parameter on the main diagonal. The narrow peaks for dip, opening (U), horizontal location (x, y), and azimuth, show that these parameters are well constrained. Depth, length and width are less well constrained by the data. The combined probability functions in the off-diagonal fields of Figure A.34 show tradeoffs between depth and length and width, but - taking the value ranges into account - still within narrow margins of 10s to 100s of meters.

It is important to note that the misfit space described by these modeling experiments is nonconvex, with multiple local minima for the dike model. Hence, the convergent solution depends on the initial model, which we prescribed as a 500 by 500 m dike 500 m below Erebus' summit. If set away from the central region, the solution tends to converge at a location at 5 km depth on the western flanks between HOOZ and CONG. This is predominantly driven by data from CONG. If we remove this station, the minimum in the misfit space is closer to the crater, but may still vary by 100s of meters in location and depth. The posterior distributions of the Bayesian inversion illustrate this complexity (Fig. A.34). Thus, we rely on prior knowledge about the shallow magmatic system (Chaput et al., 2012; Zandomeneghi et al., 2013) to set appropriate initial conditions.

Tests with different geometries, either just with the horizontal velocity field, or full observations yield poorer data fits. For example, we show the model predictions for a pressure point source (Mogi, 1958) in Fig. A.35. Here, we use the full velocity field in the inversion. While the verticals are perhaps acceptably fit, the horizontal velocities are largely underpredicted.

5.4. Deflation from November 2004 – November 2011

The velocity field spanning the time period from November 2004 until November 2011 shows clear radial inward motion toward the crater system at all continuous GNSS stations. We again test a wide range of models, including multi-source models, that include the dike resolved from the pre-2004 data and allow for slight variations in its location. Despite all the efforts, it was difficult to find a simple analytical model that captures all observations well. Figure 9 offers a simple pressure point source solution and illustrates these problems. This source is at 0.8 km asl below the Side Crater and changes in volume by about 165,000 m^3/yr (see Table 4), a similar location as the pressure point source model for the pre-2004 data. While this captures the overall characteristics of the velocity field, the vertical deformation is overpredicted, the horizontal velocity at NAUS is underpredicted, and the far field sites ABBZ and HOOZ are not well captured.

We find similar issues with other source geometries and even using two loosely bounded sources simultaneously and models that include a relatively tightly constrained dike from the pre-2004 time frame with an additional source. We offer three reasons for this misfit: (1) multiple components of the shallow magmatic system are likely active at the same time (some of our models suggest deflation of conduit-like features), (2) the summit plateau stations are all very close to this shallow system, making them very sensitive to small scale details that are perhaps not well captured in the analytical source representations or the homogeneous elastic halfspace assumptions that underlie them (Masterlark, 2007), and (3) while topography likely does not substantially influence the summit sites, sites further away (ABBZ, HOOZ) could be impacted by such effects.

The timeseries for all these stations also do not all show similar behavior. NAUS, for instance, presents relatively constant southward motion whereas CONG and MACG appear to experience two pulses of westward motion during the same time interval (Fig. 3). Linking the deflation to the magmatic system is very appropriate, however, as Knox et al. (2018) clearly show elevated explosive activity for the 2003–2011 time period, with especially high numbers of explosions detected in the seismic record for 2006 and 2007 (Fig. 3). Interestingly, these stark peaks in explosive activity are not directly mirrored in the geodetic observations. The Jones et al. (2015) terrestrial laser scanning study of crater topography highlights a consistent (2001-2010) elevation reduction in the Inner Crater, with particular features showing elevation reductions of 23.7 m for the depression hosting the lava lake and 27.1 m for the lava lake itself. Assuming a magma-static system, magma density $\rho = 2600\,\text{kg/m}^3$ and acceleration due to gravity of $g = 9.81\,\text{m/s}^2$, this would correspond to a pressure change $dP = \rho * g * h$ of about 0.68 MPa. Although the pressure point source we resolve is not finite, we can still test what initial volume we would need to match the magma-static pressure change. If we assume a shear modulus, μ, of 30 GPa and use the volume change $dV = -164,707\,\text{m}^3$ we resolve for this time period, we can solve for the required radius a to match the pressure change using $dP = (dV\mu)/(\pi a^3)$. A radius of about 1.3 km would yield a similar pressure change. Although this is very geometry dependent, and the seismic tomography did not resolve a volume of this size at the location we infer, a connection between magma-static, lake level reduction driven pressure change and pressure changes within the magmatic system are very comparable.

5.5. Inflation from November 2020 – March 2022

The inflation that started in November 2020 is remarkable as it generates the largest velocities observed at Erebus to date. We examined a range of models, as we did for previous years and find that a long and thin spheroid (Yang et al., 1988) provides one possible solution (Fig. 10). This solution is interesting as it suggests a centroid at about 136 m bsl with a semi-major axis length of 2.75 km, reaching to the bottom of the shallow magma reservoir (Fig. 11), and a semi-minor axis that is 5–6 m. In essence a conduit, centered approximately below NAU2 and near vertical with an 83° dip, striking 194° from north. If we solve for just the opening of the dike resolved for the pre-2004 period, holding all other parameters fixed, and simultaneously invert for an additional spheroid, it gets shorter and slightly thicker: the centroid is at

0.75 km depth, the semi-major axis is about 700 m and the semi-minor axis is about 10 m. The dip reduces to 73°, striking 53° from north. The fit to the data is slightly worse for this more complicated model (Figure A.36), but we consider it a notable alternative to the single spheroid model as it suggests reactivation of a previously resolved component of the shallow magmatic system with about similar opening rate (0.36 m/yr). If, similar to the pre-2004 period, we employ a Bayesian MCMC inversion for the dike model, we find that most parameters are well constrained except width and length, and tradeoffs exist for opening and length (Fig. A.36).

As discussed for the previous deformation episodes, the data are not perfectly fit, but we consider the fits adequate based on minimizing the residual norm while considering measurement uncertainties, and the unmodeled superimposed processes that affect the data. The horizontals, except for BOM2 are essentially within the small data uncertainties, as are the verticals at NAU2, CON2, and HOG2. PHIG is perhaps a bit underpredicted and BOM2 and ABBZ are not well matched. However, the deformation does agree with a shallow crustal pressurization, either gas or magma driven, perhaps foreshadowing the preparation for a new phase of higher explosive activity as observed in 1984, 2006 and 2007 (Knox et al., 2018, and our Figure3) that will likely be accompanied by renewed deflation, hopefully further elucidating the shallow magmatic system.

5.6. Magmatic Source Modeling Summary

We interpret the modeling results for the pre-2004 inflation period to indicate shallow pressurization and/or geometric modification of the shallow magmatic system. As this narrow dike terminates into the seismically imaged (Chaput et al., 2012; Zandomeneghi et al., 2013) near-summit magma reservoir (Fig. 11), we may be observing the preparation of a period of higher activity as evident in the edifice-wide deflation, increased radiant flux, and increased seismicity (Fig. 3) in the following years. However, a recharge pulse into the conduit system connecting the seismically imaged shallow magma reservoir to the NW of the crater system to the active lava lake is another possibility.

For the 2004-2011 time period we propose deflation within the shallow magmatic system that can be approximated by a pressure point source at 0.8 km asl below the Side Crater. However, as this source does not seem to integrate well with the rest of the imaged magmatic system (Fig. 11) and the source model predictions do not fit the data very well, the observed

time period	preferred model	parameter
pre-2004	Okada (1992)	longitude = 167.15088 latitude = -77.52380 depth = 663 m below reference surface (2722 m) elevation = 2059 m asl length = 150 m width = 1027 m opening = 0.32 m strike = 120° from N dip = 90° ΔV= 49,296 m^3
2004 – 2011	Mogi (1958)	longitude = 167.14866 latitude = -77.52896 depth = 2130 m below reference surface (2953 m) elevation = 823 m asl ΔV= -164,707 m^3
2020 – 2022	Yang et al. (1988)	longitude = 167.14368 latitude = -77.52555 depth = 2780 m below reference surface (2644 m) elevation = 136 m bsl semi-major= 2762 m semi-minor= 5.6 m $\Delta V*$ = 552,735 m^3 strike = 195° from N dip = 83°

Table 4: Analytical source model parameter estimates. ∗estimated following Amoruso and Crescentini (2009). Depths reference surfaces are average station elevations used in the respective inversion, topographic elevation is the difference between reference surface and depth.

deformation is likely a more complicated combination of several components the magma-reservoir – conduit – lava lake system that may benefit from more detailed numerical modeling with a particular emphasis on pressure reduction due to degassing (e.g., Shreve et al., 2022).

Similarly to the pre-2004 period we find that a shallow magma reservoir terminating conduit structure fits the 2020-2022 inflation period data best (Fig. 11). The location of these two inflation structures is relatively similar, although distinctly resolved by different geometries. Given the relatively small deformation rates, this may be due to a range of uncertainties in the observations, changes in the observation geometry, or indeed activation of discrete parts of the magma-reservoir terminating conduit system.

Thus, the picture that arises from the geodetic modeling is one of prolonged recharge of the shallow magma reservoir pressurizing its base, that must internally be compensated by changes in lava lake levels as we do not resolve additional shallower pressure-driven shallower deformation. It appears this recharge occurs via an episodic activation of a conduit system below 2,500 m extending perhaps to more than 1,000 m bsl, in its extent congruent with the chimney-like conduit system imaged by Blondel et al. (2018). The deflation appears the product of likely several more diffuse superimposed deformation sources that - while modeled with a pressure point source - is likely calling for more a complicated geometry to more appropriately reproduce the observations.

6. Conclusions

We have collected, analyzed, and modeled more than 20 years of campaign and continuous GNSS data at Erebus volcano on Ross Island, Antarctica. This is the most complete and first comprehensive geodetic analysis of GNSS data at this iconic open-vent volcanic system with a persistent convecting phonolite lava lake. Early campaign observations of the entire network, and later campaigns at the perimeter benchmarks have been critical to resolve the observed deformation. The data reveal a dynamic system that shows long-term subsidence of the volcano and Ross Island broadly due to the load of the volcanic edifice upon the Terror Rift lithosphere. Cycles of inflation and deflation are interpretable in terms of observed eruptive activity.

A first-order isostatic adjustment model shows that the long-term growth of Erebus and associated crustal loading explains some of the observed long-wavelength subsidence. Further work is required to build a more comprehensive load history and distribution, and to combine this with relevant GIA models for the region to better resolve and understand the underlying rheology and the observed subsidence.

Although the analytical magmatic source modeling does not fit all data, our results do suggest prolonged recharge of the shallow, seismically imaged magma reservoir (Zandomeneghi et al., 2013). A thin conduit system that terminates at and pressurizes the base of this magma reservoir is resolved as extending to several kilometers depth. The spatial proximity between the sources for the two inflation pulses is intriguing, suggesting a repeated process that activated the same source region.

Our analysis illustrates the value of long-term and campaign-aided high-accuracy GNSS observations at open-vent volcanoes, here enabled by exceptional progress in the engineering of polar geophysical observation systems and improved geodetic data analysis. The resolved multi-year cycles of near-vent inflation and deflation further illuminate the dynamic shallow magmatic system and motivate continued observations and time-dependent magmatic system studies at Erebus. We expect that more detailed, numerical modeling that takes into account shallow heterogeneous properties of the crust, topography, and is based on data carefully corrected for GIA and volcanic loading deformation (e.g., Grapenthin et al., 2010) will likely reduce the uncertainties in future models.

7. Acknowledgements

GPS observations at the environmentally challenging Erebus volcano were possible because of the continual and remarkable support of UNAVCO Polar personnel who installed and maintained most of the permanent continuous stations and provided instruction and instrumentation for the campaign observations. RG is particularly grateful for all the help received from Thomas Nylen and Joe Pettit. Much of the data discussed here were collected through long-term observations of the Mount Erebus Volcano Observatory (MEVO) and precursory field programs managed by the New Mexico Institute of Mining and Technology. MEVO started in 1995 and continued until December 2016 when the observatory was dismantled. PK acknowledges the following recent NSF grants for support of MEVO and on-going research at Erebus (ANT1142083, PLR1644234). This work was further supported by NSF-OPP grants 2039432 & 2026716, (RG), 1916978 (RA), and 1917178 (JC). GNSS services were provided by the Geodetic Facilities for the Advancement of Geoscience (GAGE) award, operated by UNAVCO, Inc., with support from the National Science Foundation, the National Aeronautics and Space Administration, and the U.S. Geological Survey under NSF Cooperative Agreement EAR-1724794. Geospatial support for this work provided by the Polar Geospatial Center under NSF-OPP awards 1043681 and 1559691. All the data used here are archived at UNAVCO and available for public use. The time series with respect to stable Antarctica (e.g., Figure 3) have been archived at zenodo with DOI 10.5281/zenodo.7191426.

8. Figures

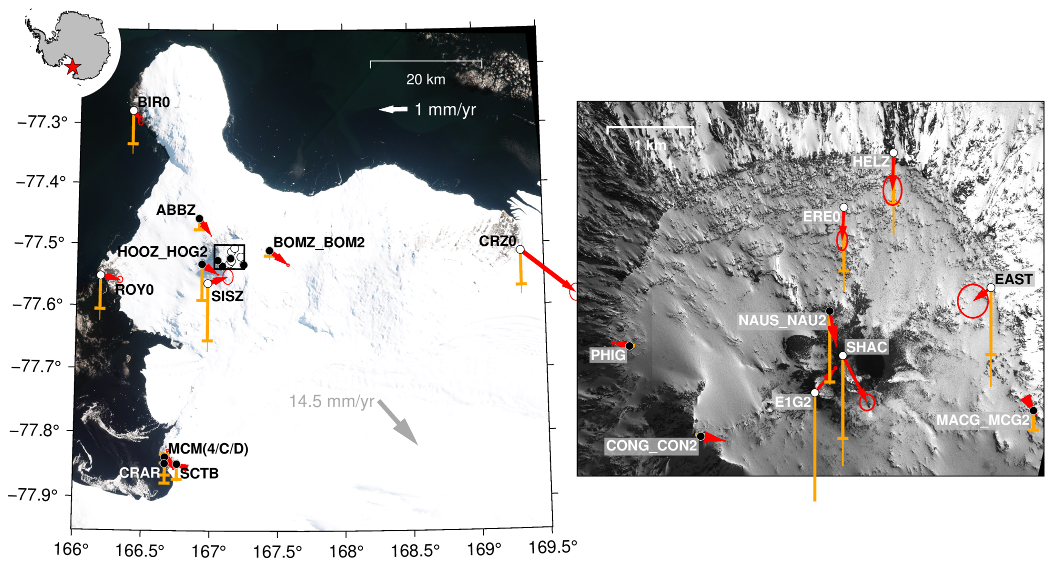

Figure 1: Map of Ross Island, Antarctica, with GNSS network and velocities over each station's lifetime as given in Fig.3 between 1995-2022. **Small inset** in top left shows Antarctica; red star marks location of Ross Island. **Main map** shows continuous GNSS stations marked by black circles, campaign GNSS stations are marked by white circles. Station names are standard four character ids, except in cases where a new monument replaced the older one, here the station name is "OLD_NEW" four character id. Antarctic plate velocity (gray vector) has been removed from the long-term GNSS velocities (red - horizontal, orange - vertical). U.S. McMurdo Station is near CRAR and MCM4. New Zealand Scott Base is at SCTB. Black rectangle shows location of inset. Background is 10 m resolution RGB color Sentinel 2 mosaic of Ross Island provided by Polar Geospatial Center. **Right inset** shows the GNSS stations and their long-term velocities with plate motion removed. Background image is 50 cm resolution panchromatic imagery of Ross Island provided by Polar Geospatial Center.

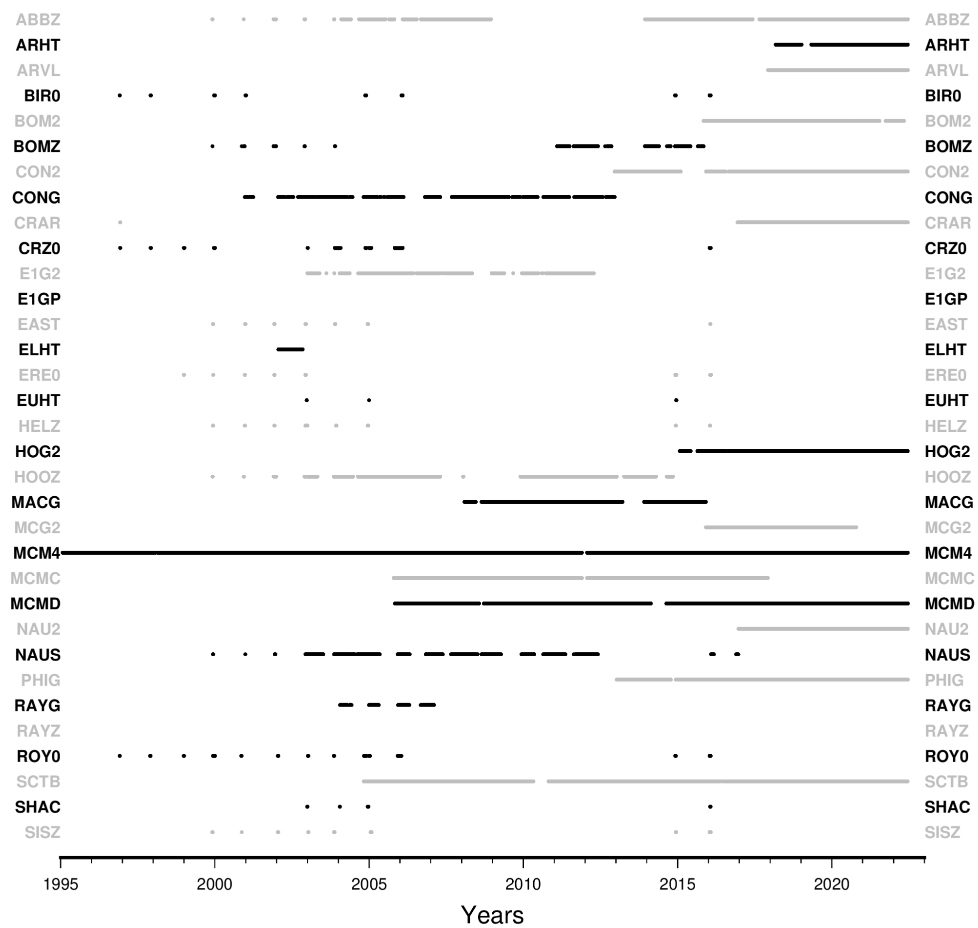

Figure 2: Times with dual frequency GNSS solutions for continuous sites ABBZ (Kyle, 2003b), ARHT (Operators, 2018), ARVL (Community, 2017b), BOM2 (Kyle, 2015), BOMZ (Kyle, 2003c), CON2 (Community, 2012), CONG (Kyle, 2000a), CRAR (Community, 2017a), E1G2 (Kyle, 2003a), HOG2 (Community, 2015a), HOOZ (Kyle, 2000b), MACG (Kyle, 2008a), MCG2 (Community, 2015b), MCM4 (Operators, 2005), MCMC (Operators, 2008), MCMD (Johns, 2006), NAU2 (Community, 2016), NAUS (Kyle, 2001a), PHIG (Kyle, 2013; Community, 2013), RAYG (Kyle, 2004a), SCTB (Blick, 2010) and campaign observations at sites BIR0, CRZ0, EAST, ELHT, ERE0, EUHT, HELZ, RAYZ, ROY0, SHAC, SISZ (Kyle, 1996; Kyle and Johns, 1996; Kyle, 1998, 2000c, 2001b, 2002, 2003d, 2004b, 2005, 2006, 2007, 2008b, 2009; Grapenthin and Kyle, 2021, 2016) gray and black colors are alternated for clarity. Periods of clearly corrupted data and single frequency observations are not included.

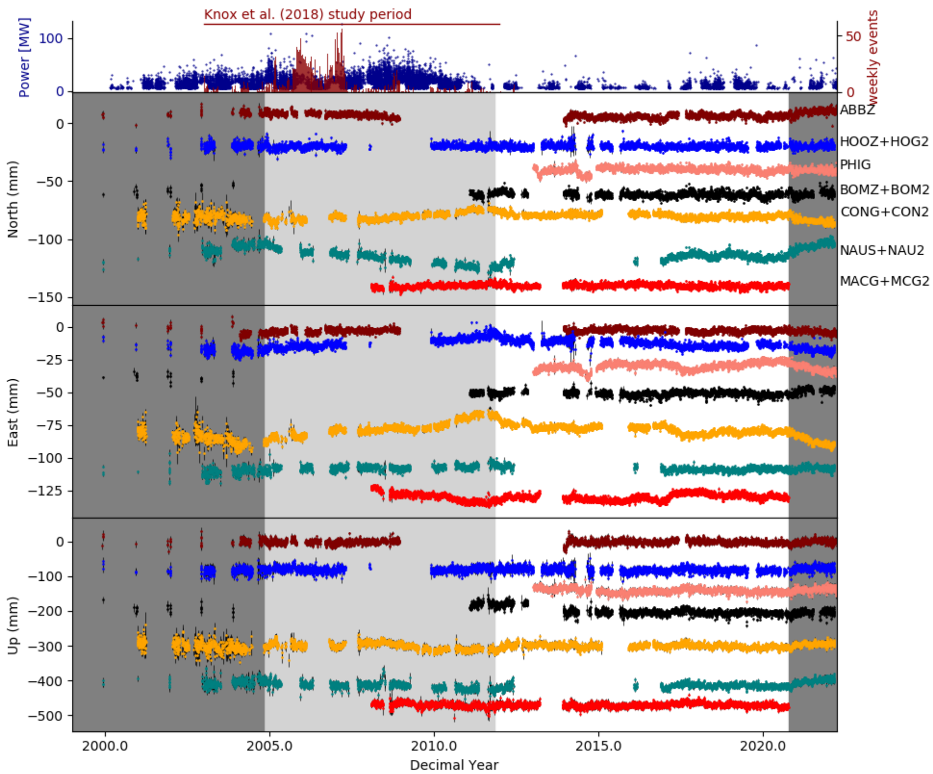

Figure 3: (Top Panel) Red bars show weekly explosion count inferred from seismic and infrasonic data between 2003 and 2011 from Knox et al. (2018). Blue dots show MODIS-derived radiative power from 2000 until 2022 using MODVOLC (Wright, 2016). Both correlate with the geodetically observed ground motions during the respective study periods, see bottom panels. (Bottom Three Panels) GNSS Time series for the continuous summit sites with respect to stable Antarctica. Panels show north, east and vertical components from top to bottom. Time series are shifted for clarity and labeled with station names in north panel, order and colors are consistent in the other two panels. Stations names of the form "xxxx+yyyy" indicate tied time series where the older station has been replaced by a newer polar mast monument. Dark gray background indicates inferred periods of inflation (until November 2004 and beginning in October 2020). Light gray background shows inferred period of deflation (approximately from November 2004 until November 2011). The respective velocities for those periods are presented in Figs. 4, 5, and 6. White background indicates an inferred time period of relative quiescence (reflected in low radiant flux above). Steps in time series at transitions from campaign observations to continuous are likely a metadata issue. These artifacts have been estimated in the processing for ABBZ, NAUS, and CONG.

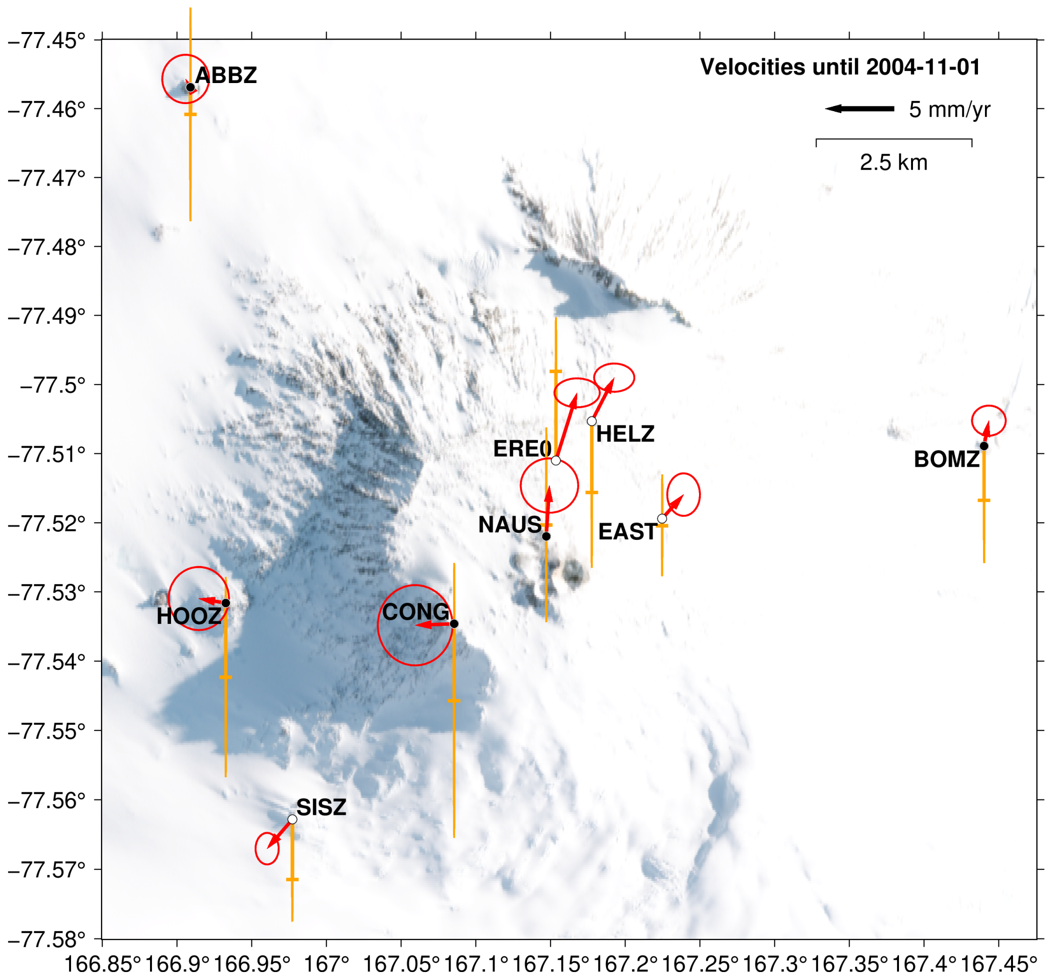

Figure 4: Velocities for the period before 2004-11-01 for stations with data of more than 1 year. Red arrows indicate horizontal velocity and orange bars indicate vertical velocity (up on the figure indicates upward velocity and zero velocity is at the station location). The velocity magnitude scale is indicated by the horizontal arrow in the legend. Horizontal error ellipses and orange vertical bar extents indicate 95 % confidence intervals.

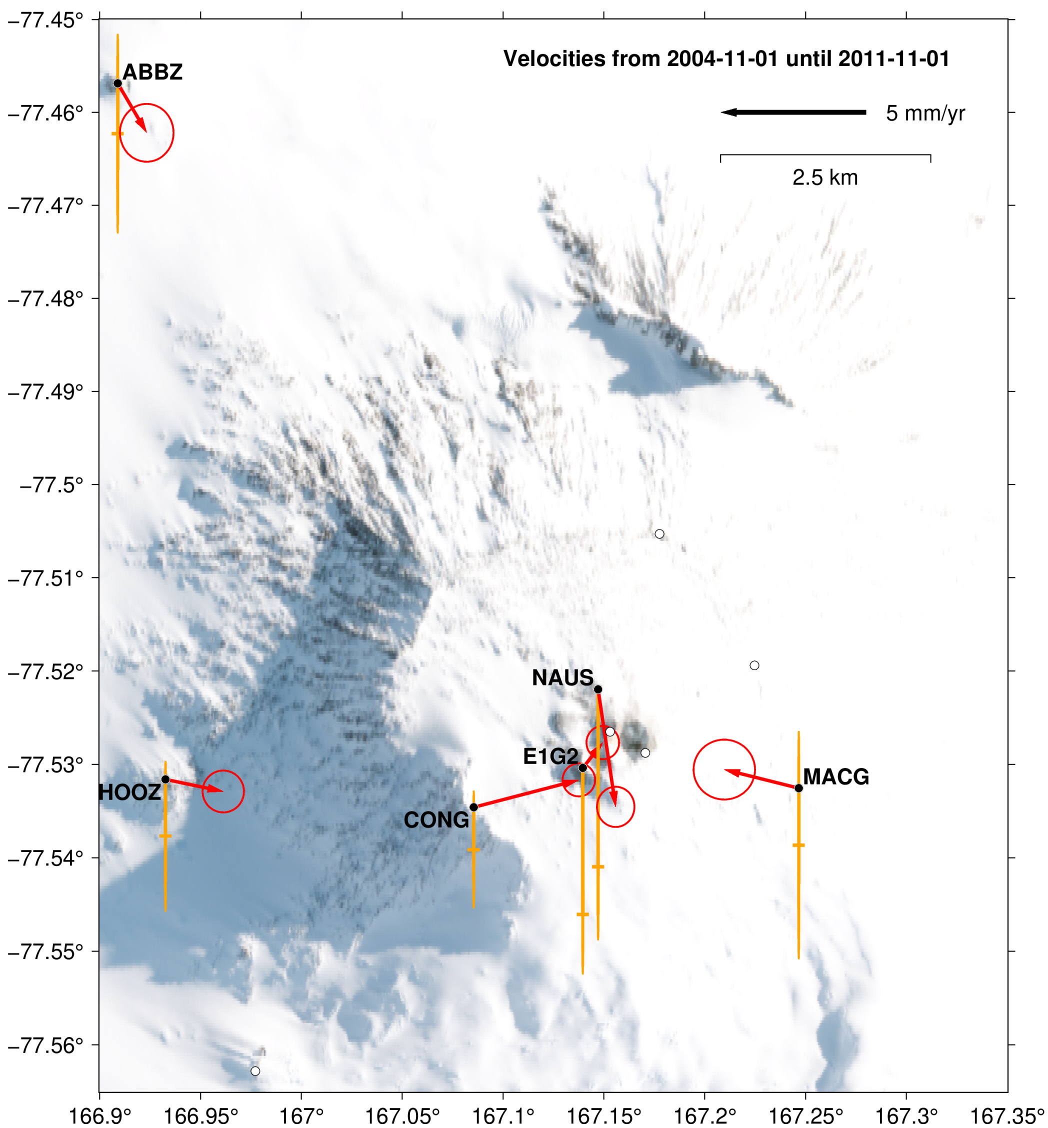

Figure 5: Velocities estimated for 2004-11-01 to 2011-11-01.

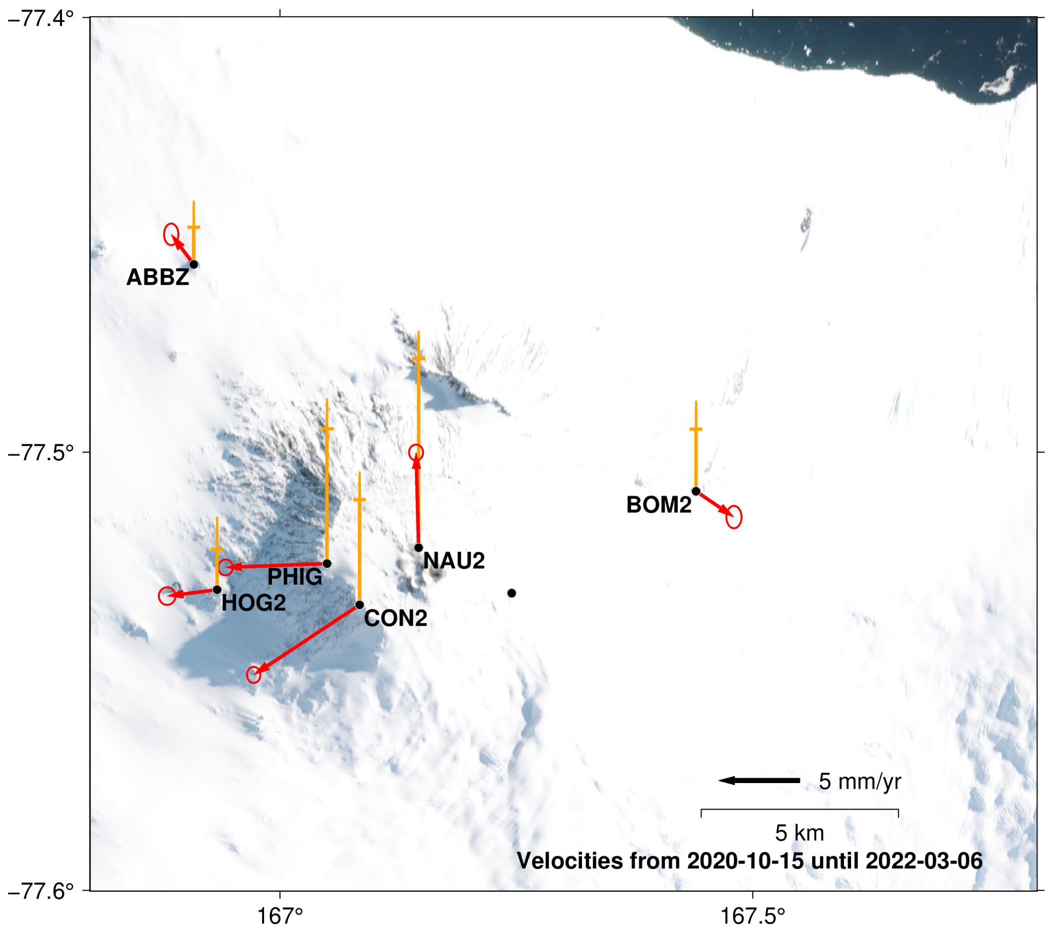

Figure 6: Velocities for 2020-10-15 – 2022-03-06.

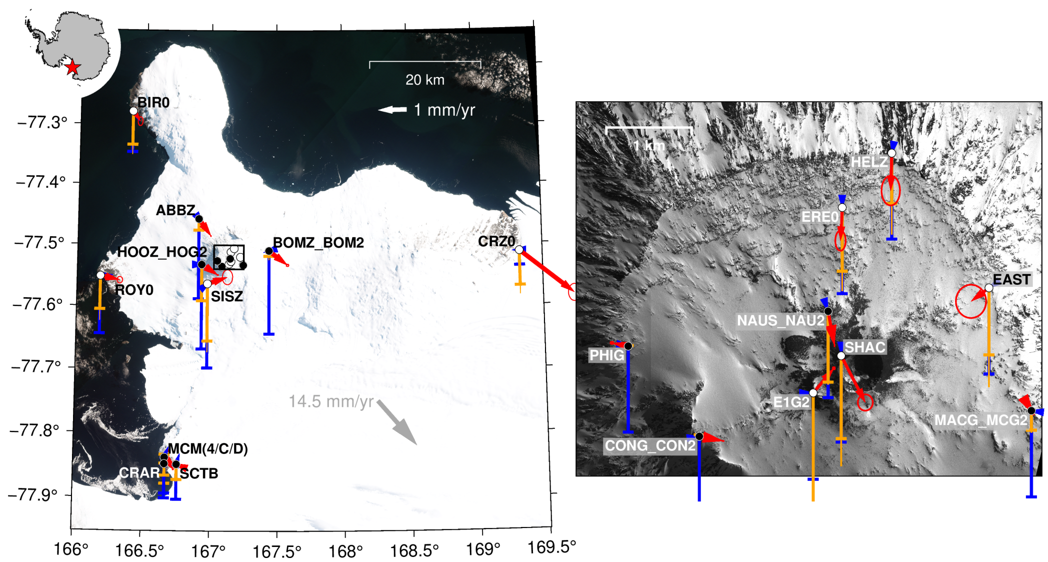

Figure 7: Like Figure 1, but blue vectors show modeled isostatic adjustment due to 4 km^3 of lava added over a 3 km radius onto the summit plateau every 1000 yrs. The model assumes an elastic plate with Young's modulus of 80 GPa and a Poisson's ratio of 0.25 over a half space with a viscosity of $1 \times 10^1 9$ Pa s.

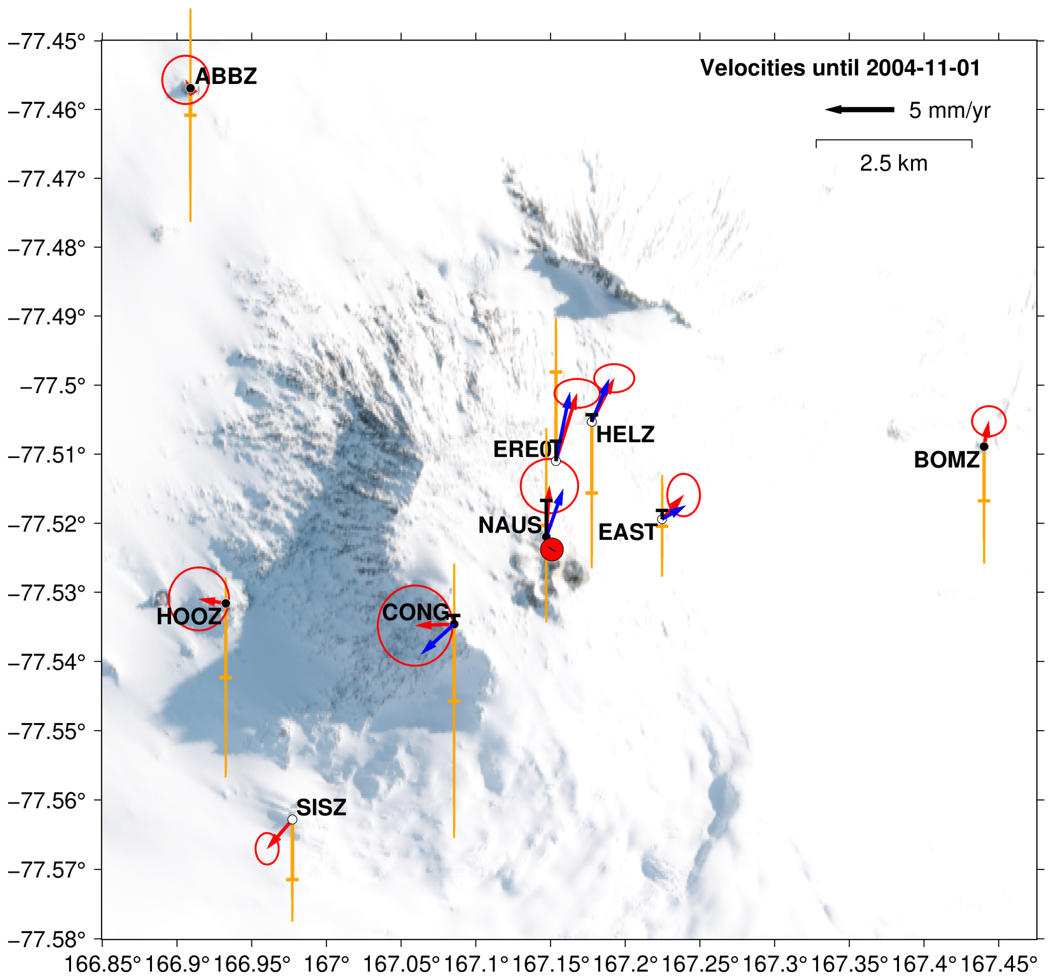

Figure 8: Model fit and residuals for the period before November 2004. Data are red (horizontal) and orange (vertical). Model predictions (negligible at peripheral stations ABBZ, HOOZ, SISZ, and BOMZ) are blue (horizontal) and black (vertical). The red circle indicates the map location of the source centroid (the thin black line inside the circle marks orientation and length of the model dike). Model parameters are listed in Table 4.

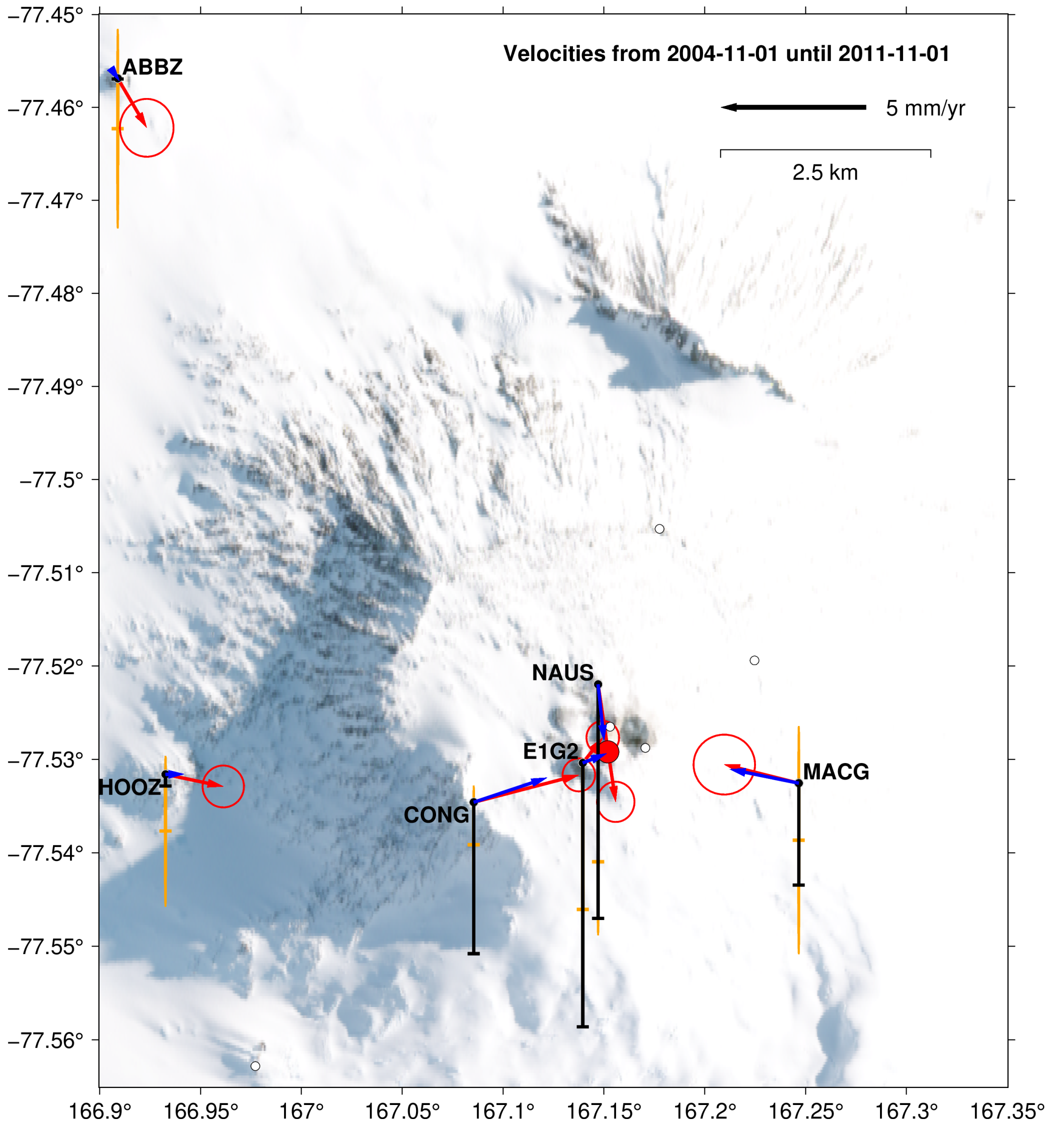

Figure 9: Same as Fig. 8 but for 2004 – 2011.

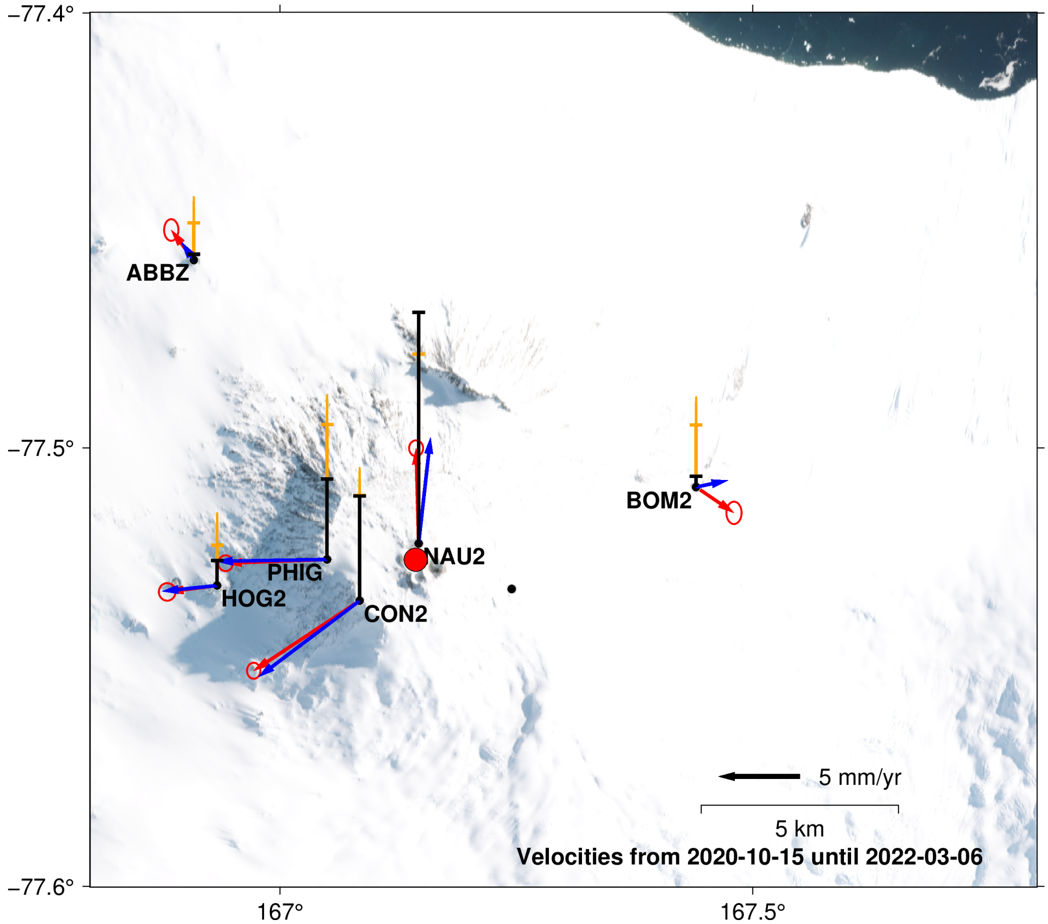

Figure 10: Same as Fig. 8, but for 2020 – 2022.

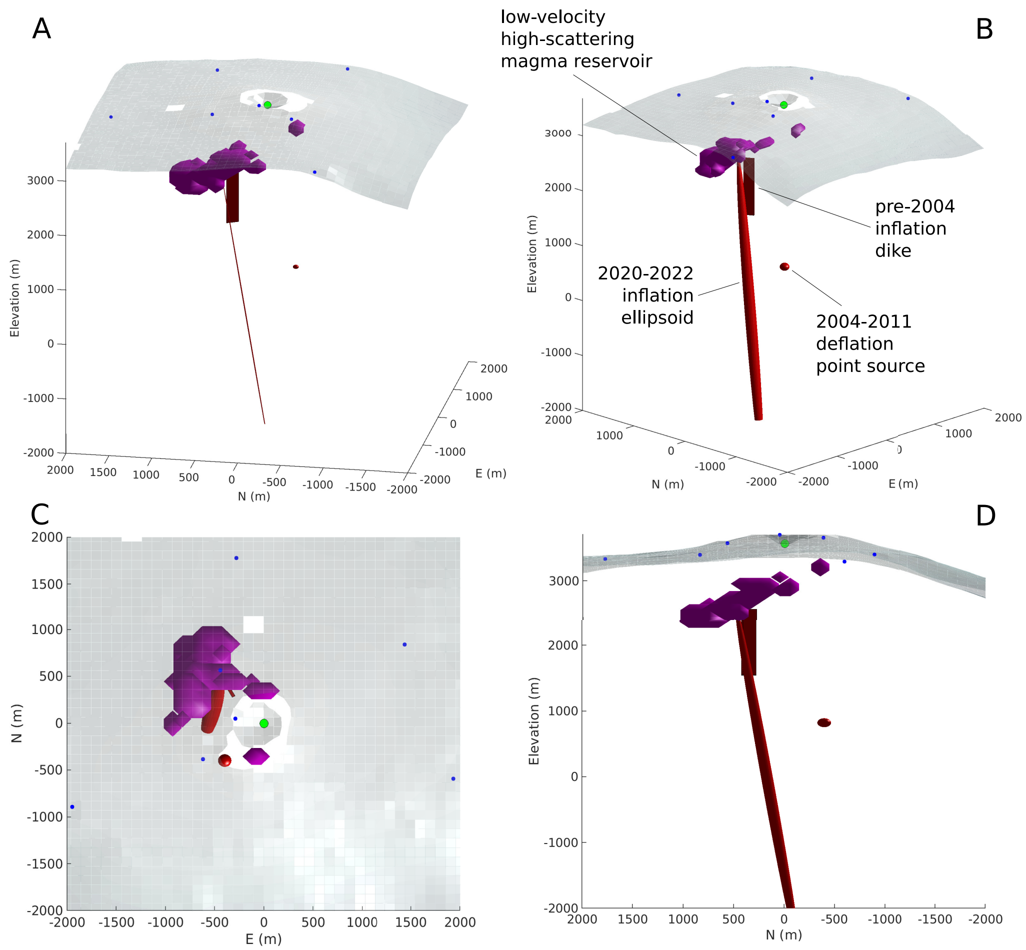

Figure 11: Geodetic source models (red) in the context of the Zandomeneghi et al. (2013) low-velocity high-scattering magma reservoir (purple). GNSS stations are blue dots, green circle indicates lava lake location. **(A)** Narrow and tall dike next to thin and elongated elongated ellipsoid represent magma-reservoir terminating lower conduit structures. The 2004 - 2011 Mogi source is off to the side near 800 m elevation. Dimensions are to scale. **(B)** Source thicknesses are exaggerated for visibility: Mogi source with doubled radius, ellipsoid semi-minor axes lengths are multiplied by 10, and dike opening is multiplied by 100. **(C)** Same as B, but in map view. **(D)** Same as B, but in cross-section looking to the east.

References

Agnew, D.C., 2012. SPOTL: Some Programs for Ocean-Tide Loading. Technical Report. Scripps Institution of Oceanography. La Jolla.

Altamimi, Z., Rebischung, P., Métivier, L., Collilieux, X., 2016. ITRF2014: A new release of the International Terrestrial Reference Frame modeling nonlinear station motions. Journal of Geophysical Research: Solid Earth 121, 6109–6131. doi:10.1002/2016JB013098.

Amoruso, A., Crescentini, L., 2009. Shape and volume change of pressurized ellipsoidal cavities from deformation and seismic data. Journal of Geophysical Research 114, B02210. doi:10.1029/2008JB005946.

Argus, D.F., Gordon, R.G., Heflin, M.B., Ma, C., Eanes, R.J., Willis, P., Peltier, W.R., Owen, S.E., 2010. The angular velocities of the plates and the velocity of Earth's centre from space geodesy. Geophysical Journal International 180, 913–960. doi:10.1111/j.1365-246X.2009.04463.x.

Aster, R., 2003. Very long period oscillations of Mount Erebus Volcano. Journal of Geophysical Research 108, 2522. doi:10.1029/2002JB002101.

Aster, R., McIntosh, W., Kyle, P., Esser, R., Bartel, B., Dunbar, N., Johns, B., Johnson, J., Karstens, R., Kurnik, C., McGowan, M., McNamara, S., Meertens, C., Pauly, B., Richmond, M., Ruiz, M., 2004. Real-time data received from Mount Erebus volcano, Antarctica. Eos 85. doi:10.1029/2004EO100001.

Aster, R.C., Borchers, B., Thurber, C.H., 2018. Parameter Estimation and Inverse Problems. 3rd ed. ed., Elsevier.

Bannister, S., Yu, J., Leitner, B., Kennett, B.L., 2003. Variations in crustal structure across the transition from West to East Antarctica, Southern Victoria Land. Geophysical Journal International 155, 870–880. doi:10.1111/j.1365-246X.2003.02094.x.

Barbot, S., Fialko, Y., 2010a. Fourier-domain Green's function for an elastic semi-infinite solid under gravity, with applications to earthquake and volcano deformation. Geophysical Journal International 182, 568–582. doi:10.1111/j.1365-246X.2010.04655.x.

Barbot, S., Fialko, Y., 2010b. A unified continuum representation of post-seismic relaxation mechanisms: Semi-analytic models of afterslip, poroelastic rebound and viscoelastic flow. Geophysical Journal International 182, 1124–1140. doi:10.1111/j.1365-246X.2010.04678.x.

Behrendt, J.C., 1999. Crustal and lithospheric structure of the west Antarctic Rift System from geophysical investigations - A review. Global and Planetary Change 23, 25–44. doi:10.1016/S0921-8181(99)00049-1.

Bertiger, W., Bar-Sever, Y., Dorsey, A., Haines, B., Harvey, N., Hemberger, D., Heflin, M., Lu, W., Miller, M., Moore, A.W., Murphy, D., Ries, P., Romans, L., Sibois, A., Sibthorpe, A., Szilagyi, B., Vallisneri, M., Willis, P., 2020. GipsyX/RTGx, a new tool set for space geodetic operations and research. Advances in Space Research 66, 469–489. doi:10.1016/j.asr.2020.04.015.

Biggs, J., Pritchard, M.E., 2017. Global Volcano Monitoring: What Does It Mean When Volcanoes Deform? Elements 13, 17–22. doi:10.2113/gselements.13.1.17.

Blick, G., 2010. Antarctica-POLENET GPS Network: SCTB-Scott Base GPS P.S. doi:10.7283/T5CF9N6P.

Blick, G.H., Otway, P.M., Scott, B.J., 1989. Deformation Monitoring of Mt. Erebus, Antarctica, 1980–1985, in: Latter, J.H. (Ed.), IAVCEI Proceedings in Volcanology 1. Springer-Verlag, Berlin Heidelberg, pp. 554–560. doi:10.1007/978-3-642-73759-6_32.

Blondel, T., Chaput, J., Derode, A., Campillo, M., Aubry, A., 2018. Matrix Approach of Seismic Imaging: Application to the Erebus Volcano, Antarctica. Journal of Geophysical Research: Solid Earth 123, 10,936–10,950. doi:10.1029/2018JB016361.

Böhm, J., Möller, G., Schindelegger, M., Pain, G., Weber, R., 2015. Development of an improved empirical model for slant delays in the troposphere (GPT2w). GPS Solutions 19, 433–441. doi:10.1007/s10291-014-0403-7.

Bouche, E., Vergniolle, S., Staudacher, T., Nercessian, A., Delmont, J.C., Frogneux, M., Cartault, F., Le Pichon, A., 2010. The role of large bubbles detected from acoustic measurements on the dynamics of Erta 'Ale lava lake (Ethiopia). Earth and Planetary Science Letters 295, 37–48. doi:10.1016/j.epsl.2010.03.020.

Chaput, J., Zandomeneghi, D., Aster, R.C., Knox, H., Kyle, P.R., 2012. Imaging of Erebus volcano using body wave seismic interferometry of Strombolian eruption coda. Geophysical Research Letters 39. doi:10.1029/2012GL050956.

Chaussard, E., Amelung, F., Aoki, Y., 2013. Characterization of open and closed volcanic systems in Indonesia and Mexico using InSAR time series. Journal of Geophysical Research: Solid Earth 118, 3957–3969. doi:10.1002/jgrb.50288.

Community, U., 2012. Antarctica-Erebus GPS Network: CON2-Truncated_Cones_GPS_2 P.S. doi:10.7283/T54M92XM.

Community, U., 2013. Antarctica-Erebus GPS Network: PHIG-Mount Erebus West GPS P.S. doi:10.7283/T5SF2TKR.

Community, U., 2015a. Antarctica-Erebus GPS Network: HOG2-Hooper_Shoulder_ P.S. doi:10.7283/T5HX1B3N.

Community, U., 2015b. Antarctica-Erebus GPS Network: MCG2-MacIntosh_Ridge2 P.S. doi:10.7283/T50V8B69.

Community, U., 2016. Antarctica-Erebus GPS Network: NAU2-NauseaKnobErebus P.S. doi:10.7283/T51V5CBP.

Community, U., 2017a. Antarctica-Infrastructure GPS Network - CRAR-McMurdo_CraryLab P.S. doi:10.7283/CQF7-N229.

Community, U., 2017b. Antarctica-Infrastructure GPS Network: ARVL-Arrival_Heights_ P.S. doi:10.7283/T5T43RWJ.

Dibble, R., Kyle, P., Rowe, C., 2008. Video and seismic observations of Strombolian eruptions at Erebus volcano, Antarctica. Journal of Volcanology and Geothermal Research 177, 619–634. doi:10.1016/j.jvolgeores.2008.07.020.

Dibble, R.R., Kienle, J., Kyle, P.R., Shibuya, K., 1984. Geophysical studies of erebus volcano, Antarctica, from 1974 december to 1982 january. New

Zealand Journal of Geology and Geophysics 27, 425–455. doi:10.1080/00288306.1984.10422264.

Donnellan, A., Luyendyk, B.P., 2004. GPS evidence for a coherent Antarctic plate and for postglacial rebound in Marie Byrd Land. Global and Planetary Change 42, 305–311. doi:10.1016/j.gloplacha.2004.02.006.

Dow, J.M., Neilan, R.E., Rizos, C., 2009. The International GNSS Service in a changing landscape of Global Navigation Satellite Systems. J. Geod. 83, 191–198. doi:10.1007/s00190-008-0300-3.

Dzurisin, D., 2007. Volcano Deformation. Springer-Praxis, Chichester, UK.

Edmonds, M., Liu, E.J., Cashman, K.V., 2022. Open-vent volcanoes fuelled by depth-integrated magma degassing. Bulletin of Volcanology 84. doi:10.1007/s00445-021-01522-8.

Egbert, G.D., Erofeeva, S.Y., 2002. Efficient inverse modeling of barotropic ocean tides. Journal of Atmospheric and Oceanic Technology 19, 183–204. doi:10.1175/1520-0426(2002)019<0183:EIMOBO>2.0.CO;2.

Esser, R.P., Kyle, P.R., McIntosh, W.C., 2004. 40 Ar/ 39 Ar dating of the eruptive history of Mount Erebus, Antarctica: Volcano evolution. Bulletin of Volcanology 66, 671–686. doi:10.1007/s00445-004-0354-x.

Fialko, Y., Simons, M., 2001. Evidence for on-going inflation of the Socorro magma body, New Mexico, from interferometric synthetic aperture radar imaging. Geophysical Research Letters 28, 3549–3552. doi:10.1029/2001GL013318.

Fielding, C.R., Whittaker, J., Henrys, S.A., Wilson, T.J., Naish, T.R., 2008. Seismic facies and stratigraphy of the Cenozoic succession in McMurdo Sound, Antarctica: Implications for tectonic, climatic and glacial history. Palaeogeography, Palaeoclimatology, Palaeoecology 260, 8–29. doi:10.1016/j.palaeo.2007.08.016.

Fu, Y., Freymueller, J.T., van Dam, T., 2012. The effect of using inconsistent ocean tidal loading models on GPS coordinate solutions. Journal of Geodesy 86, 409–421. doi:10.1007/s00190-011-0528-1.

Gerst, A., Hort, M., Aster, R.C., Johnson, J.B., Kyle, P.R., 2013. The first second of volcanic eruptions from the Erebus volcano lava lake, Antarctica - Energies, pressures, seismology, and infrasound. Journal of Geophysical Research: Solid Earth 118, 3318–3340. doi:10.1002/jgrb.50234.

Giggenbach, W.F., Kyle, P.R., Lyon, G.L., 1973. Present Volcanic Activity on Mount Erebus, Ross Island, Antarctica. Geology 1, 135. doi:10.1130/0091-7613(1973)1<135:PVAOME>2.0.CO;2.

Grapenthin, R., 2014. CrusDe: A plug-in based simulation framework for composable Crustal Deformation studies using Green's functions. Computers & Geosciences 62, 168–177. doi:10.1016/j.cageo.2013.07.005.

Grapenthin, R., Freymueller, J.T., Kaufman, A.M., 2013. Geodetic observations during the 2009 eruption of Redoubt Volcano, Alaska. Journal of Volcanology and Geothermal Research 259, 115–132. doi:10.1016/j.jvolgeores.2012.04.021.

Grapenthin, R., Kyle, P., 2016. Antarctica Support 2015/2016: G-081 Kyle. doi:10.7283/T5057DBN.

Grapenthin, R., Kyle, P., 2021. Antarctica Support 2014/2015 - G-081 Kyle. doi:10.7283/10K5-MN83.

Grapenthin, R., Ófeigsson, B., Sigmundsson, F., Sturkell, E., Hooper, A., 2010. Pressure sources versus surface loads: Analyzing volcano deformation signal composition with an application to Hekla volcano, Iceland. Geophysical Research Letters 37. doi:10.1029/2010GL044590.

Henrys, S., Wilson, T., Whittaker, J.M., Fielding, C., Hall, J., Naish, T.R., 2007. Tectonic History of Mid-Miocene to Present Southern Victoria Land Basin, inferred from Seismic Stratigraphy, in McMurdo Sound, Antarctica, in: Cooper, A.K., Raymond, C.R., Al., E. (Eds.), Antarctica: A Keystone in a Changing World – Online Proceedings of the 10th ISAES, U.S. Geol. Surv. Open File Rep. 2007-1047, Short Res. Pap. 049, pp. 49–52. doi:10.3133/of2007-1047.srp049.

Hill, G.J., Wannamaker, P.E., Maris, V., Stodt, J.A., Kordy, M., Unsworth, M.J., Bedrosian, P.A., Wallin, E.L., Uhlmann, D.F., Ogawa, Y., Kyle, P., 2022. Trans-crustal structural control of CO2-rich extensional magmatic systems revealed at Mount Erebus Antarctica. Nature Communications 13, 2989. doi:10.1038/s41467-022-30627-7.

Hodge, B.E., Pettit, J., Meertens, C.M., Mattioli, G.S., Nylen, T., Bayou, N., Zaino, A., Niebuhr, S., 2018. A decade of continuous autonomous station operations in remote polar regions, in: AGU Fall Meeting Abstracts, pp. G13B—-0505.

Ivins, E.R., van der Wal, W., Wiens, D.A., Lloyd, A.J., Caron, L., 2022. Antarctic upper mantle rheology. Geological Society, London, Memoirs 56, M56–2020–19. doi:10.1144/M56-2020-19.

Jha, S., Harry, D.L., Wenman, C.P., Mayle, M., 2022. Flexural subsidence around {Ross Island, West Antarctica}. Geochemistry, Geophysics, Geosystems doi:10.1029/2021gc010181.

Johns, B., 2006. Antarctica-Infrastructure GPS Network: MCMD-McMurdo Community Base Station P.S. doi:10.7283/T5FB514D.

Jones, L.K., Kyle, P.R., Oppenheimer, C., Frechette, J.D., Okal, M.H., 2015. Terrestrial laser scanning observations of geomorphic changes and varying lava lake levels at Erebus volcano, Antarctica. Journal of Volcanology and Geothermal Research 295, 43–54. doi:10.1016/j.jvolgeores.2015.02.011.

Jordan, T.A., Riley, T.R., Siddoway, C.S., 2020. The geological history and evolution of West Antarctica. Nature Reviews Earth and Environment 1, 117–133. doi:10.1038/s43017-019-0013-6.

Kelly, P.J., Dunbar, N.W., Kyle, P.R., McIntosh, W.C., 2008. Refinement of the late Quaternary geologic history of Erebus volcano, Antarctica using 40Ar/39Ar and 36Cl age determinations. Journal of Volcanology and Geothermal Research 177, 569–577. doi:10.1016/j.jvolgeores.2008.07.018.

King, M., Santamaría-Gómez, A., 2016. Ongoing deformation of Antarctica following recent Great Earthquakes. Geophysical Research Letters 43, 1918–1927. doi:10.1002/2016GL067773.

King, M.A., Whitehouse, P.L., van der Wal, W., 2016. Incomplete separability of Antarctic plate rotation from glacial isostatic adjustment deformation within geodetic observations. Geophysical Journal International 204, 324–330. doi:10.1093/gji/ggv461.

Knox, H.A., Chaput, J.A., Aster, R.C., Kyle, P.R., 2018. Multiyear Shallow Conduit Changes Observed With Lava Lake Eruption Seismograms at Erebus Volcano, Antarctica. Journal of Geophysical Research: Solid Earth 123, 3178–3196. doi:10.1002/2017JB015045.

Kyle, P., 1996. Antarctica Support 1995/1996: S-081, Mount Erebus. doi:10.7283/T5542KQZ.

Kyle, P., 1998. Antarctica Support 1997/1998: S-081, Mt. Erebus. doi:10.7283/T5JD4TW1.

Kyle, P., 2000a. Antarctica-Erebus GPS Network: CONG-Truncated Cones P.S. doi:10.7283/T5RX996S.

Kyle, P., 2000b. Antarctica-Erebus GPS Network: HOOZ-Hooper's Shoulder P.S. doi:10.7283/T5HD7SRN.

Kyle, P., 2000c. Antarctica Support 1999/2000: G-081 Mount Erebus. doi:10.7283/T5P55KMR.

Kyle, P., 2001a. Antarctica-Erebus GPS Network: NAUS-Nausea Knob P.S. doi:10.7283/T5CN721Q.

Kyle, P., 2001b. Antarctica Support 2000/2001: G-081 Mt. Erebus. doi:10.7283/T5M61HBJ.

Kyle, P., 2002. Antarctica Support 2001/2002: G-081 Mt. Erebus. doi:10.7283/T5GF0RMT.

Kyle, P., 2003a. Antarctica-Erebus GPS Network: E1G2-E1 P.S. doi:10.7283/T57W69BF.

Kyle, P., 2003b. Antarctica L1 GPS Network: ABBZ-Abbott Peak P.S. doi:10.7283/T58W3BDX.

Kyle, P., 2003c. Antarctica L1 GPS Network: BOMZ-Bombs P.S. doi:10.7283/T5DN4353.

Kyle, P., 2003d. Antarctica Support 2002/2003: G-081 Mt. Erebus. doi:10.7283/T5BP00XX.

Kyle, P., 2004a. Antarctica-Erebus GPS Network: RAYG-Ray Seismic Site P.S. doi:10.7283/T50G3H8K.

Kyle, P., 2004b. Antarctica Support 2003/2004: G-081 Erebus. doi:10.7283/T5707ZJD.

Kyle, P., 2005. Antarctica Support 2004/2005: G-081 Mt. Erebus. doi:10.7283/T53776VH.

Kyle, P., 2006. Antarctica Support 2005/2006: G-081 Mount Erebus Volcano Observatory. doi:10.7283/T5TQ5ZNH.

Kyle, P., 2007. Antarctica Support 2006/2007: G-081 Mount Erebus Volcano Observatory. doi:10.7283/T5PZ56X5.

Kyle, P., 2008a. Antarctica-Erebus GPS Network: MACG-MacIntosh P.S. doi:10.7283/T5VQ30S8.

Kyle, P., 2008b. Antarctica Support 2007/2008: G-081 Mount Erebus Observatory. doi:10.7283/T5K64G65.

Kyle, P., 2009. Antarctica Support 2008/2009: G-081 Mt Erebus. doi:10.7283/T5FJ2DWR.

Kyle, P., 2013. Antarctica-Erebus GPS Network: PHIG-Mount Erebus West GPS P.S. doi:10.7283/T5D50KC7.

Kyle, P., 2015. Antarctica L1 GPS Network - BOM2-Erebus_BOMZ_GP2_P.S. doi:10.7283/3V25-S796.

Kyle, P., Johns, B., 1996. Antarctica Support 1996/1997: S-081, Mt. Erebus. doi:10.7283/T5MG7MMD.

Kyle, P.R., Moore, J.A., Thirlwall, M.F., 1992. Petrologic evolution of anorthoclase phonolite lavas at Mount Erebus, Ross island, Antarctica. Journal of Petrology 33, 849–875. doi:10.1093/petrology/33.4.849.

Le Losq, C., Neuville, D.R., Moretti, R., Kyle, P.R., Oppenheimer, C., 2015. Rheology of phonolitic magmas - the case of the Erebus lava lake. Earth and Planetary Science Letters 411, 53–61. doi:10.1016/j.epsl.2014.11.042.

Lev, E., Ruprecht, P., Oppenheimer, C., Peters, N., Patrick, M., Hernández, P.A., Spampinato, L., Marlow, J., 2019. A global synthesis of lava lake dynamics. Journal of Volcanology and Geothermal Research 381, 16–31. doi:10.1016/j.jvolgeores.2019.04.010.

Martin, A.P., Cooper, A.F., Price, R.C., Kyle, P.R., Gamble, J.A., 2021. Chapter 5.2b Erebus Volcanic Province: Petrology. Geological Society, London, Memoirs 55, 447–489. doi:10.1144/M55-2018-80.

Masterlark, T., 2007. Magma intrusion and deformation predictions: Sensitivities to the Mogi assumptions, J. Geophys. Res., 112, B06419 doi, 101029/.

Mitrovica, J.X., Gomez, N., Clark, P.U., 2009. The sea-level fingerprint of West Antarctic collapse. Science (New York, N.Y.) 323, 753. doi:10.1126/science.1166510.

Mogi, K., 1958. Relations between eruptions of various volcanoes and the deformations of the ground surface around them. Bull. Earthquake Res. Inst. Univ. Tokyo 36, 99–134.

Morin, R.H., Williams, T., Henrys, S.A., Magens, D., Niessen, F., Hansaraj, D., 2010. Heat flow and hydrologic characteristics at the AND-1B borehole, ANDRILL McMurdo Ice Shelf project, Antarctica. Geosphere 6, 370–378. doi:10.1130/GES00512.1.

Moussallam, Y., Oppenheimer, C., Scaillet, B., Gaillard, F., Kyle, P., Peters, N., Hartley, M., Berlo, K., Donovan, A., 2014. Tracking the changing oxidation state of Erebus magmas, from mantle to surface, driven by magma ascent and degassing. Earth and Planetary Science Letters 393, 200–209. doi:10.1016/j.epsl.2014.02.055.

Noell, S.E., Baptista, M.S., Smith, E., McDonald, I.R., Lee, C.K., Stott, M.B., Amend, J.P., Cary, S.C., 2022. Unique Geothermal Chemistry Shapes Microbial Communities on Mt. Erebus, Antarctica. Frontiers in Microbiology 13.

Okada, Y., 1992. Internal deformation due to shear and tensile faults in a half-space. Bull. Seis. Soc. Am. 82, 1018–1040.

Operators, G., 2005. GGN GNSS Network - MCM4-McMurdo GPS Station P.S. doi:10.7283/3HY6-CJ28.

Operators, G., 2008. GGN GNSS Network - MCMC-McMurdo L2C P.S. doi:10.7283/ZWER-J158.

Operators, G., 2018. GGN GNSS Network - ARHT-Arrival Heights GNSS Station P.S. doi:10.7283/J022-VF69.

Oppenheimer, C., Moretti, R., Kyle, P.R., Eschenbacher, A., Lowenstern, J.B., Hervig, R.L., Dunbar, N.W., 2011. Mantle to surface degassing of alkalic magmas at Erebus volcano, Antarctica. Earth and Planetary Science Letters 306, 261–271. doi:10.1016/j.epsl.2011.04.005.

Otway, P.M., Blick, G.H., Scott, B.J., 1994. Volcanic deformation monitoring on Mount Erebus: Methods and results of geodetic surveys, 1980–1985, in: Kyle, P.R. (Ed.), Volcanological and Environmental Studies of Mount Erebus, Antarctica, Volume 66. American Geophysical Union. volume 66, pp. 57–68. doi:10.1029/AR066p0057.

Parmelee, D.E.F., Kyle, P.R., Kurz, M.D., Marrero, S.M., Phillips, F.M., 2015. A new Holocene eruptive history of Erebus volcano, Antarctica using cosmogenic 3He and 36Cl exposure ages. Quaternary Geochronology 30, 114–131. doi:10.1016/j.quageo.2015.09.001.

Peters, N., Oppenheimer, C., Kyle, P., Kingsbury, N., 2014. Decadal persistence of cycles in lava lake motion at Erebus volcano, Antarctica. Earth and Planetary Science Letters 395, 1–12. doi:10.1016/j.epsl.2014.03.032.

Pinel, V., Jaupart, C., 2000. The effect of edifice load on magma ascent beneath a volcano. Phil. Trans. R. Soc. Lond. A 358, 1515–1532.

Pritchard, M.E., Simons, M., 2002. A satellite geodetic survey of large-scale deformation of volcanic centres in the central Andes. Nature 418, 167–171. doi:10.1038/nature00872.

Rose, W.I., Palma, J.L., Granados, H.D., Varley, N., 2013. Open-vent volcanism and related hazards: Overview. Special Paper of the Geological Society of America 498, vii–xiii. doi:10.1130/2013.2498(00).

Rowe, C.A., Aster, R.C., Kyle, P.R., Dibble, R.R., Schlue, J.W., 2000. Seismic and acoustic observations at Mount Erebus Volcano, Ross Island, Antarctica, 1994-1998. Journal of Volcanology and Geothermal Research 101, 105–128. doi:10.1016/S0377-0273(00)00170-0.

Segall, P., 2010. Earthquake and Volcano Deformation. Princeton University Press, Princeton.

Shimada, S., Fujinawa, Y., Sekiguchi, S., Ohmi, S., Eguchi, T., Okada, Y., 1990. Detection of a volcanic fracture opening in Japan using Global Positioning System measurements. Nature 343, 631–633. doi:10.1038/343631a0.

Shreve, T., Grandin, R., Boichu, M., 2022. Reservoir depressurization driven by passive gas emissions at Ambrym volcano. Earth and Planetary Science Letters 584, 117512. doi:10.1016/j.epsl.2022.117512.

Sigmundsson, F., Parks, M., Pedersen, R., Jónsdóttir, K., Ófeigsson, B.G., Grapenthin, R., Dumont, S., Einarsson, P., Drouin, V., Heimisson, E.R., Hjartardóttir, Á.R., Guðmundsson, M., Geirsson, H., Hreinsdóttir, S., Sturkell, E., Hooper, A., Högnadóttir, Þ., Vogfjörð, K., Barnie, T., Roberts, M.J., 2018. Magma Movements in Volcanic Plumbing Systems and Their Associated Ground Deformation and Seismic Patterns. Elsevier Inc. doi:10.1016/b978-0-12-809749-6.00011-x.

Sims, K.W., Pichat, S., Reagan, M.K., Kyle, P.R., Dulaiova, H., Dunbar, N.W., Prytulak, J., Sawyer, G., Layne, G.D., Blichert-Toft, J., Gauthier, P.J., Charette, M.A., Elliott, T.R., 2013. On the time scales of magma genesis, melt evolution, crystal growth rates and magma degassing in the erebus volcano magmatic system using the 238U, 235U and 232Th decay series. Journal of Petrology 54, 235–271. doi:10.1093/petrology/egs068.

Sims, K.W.W., Aster, R.C., Gaetani, G., Blichert-Toft, J., Phillips, E.H., Wallace, P.J., Mattioli, G.S., Rasmussen, D., Boyd, E.S., 2021. Chapter 7.2 Mount Erebus. Geological Society, London, Memoirs 55, 695–739. doi:10.1144/M55-2019-8.

Smellie, J.L., Martin, A.P., Panter, K.S., Kyle, P.R., Geyer, A., 2020. Magmatism in Antarctica and its relation to Zealandia. New Zealand Journal of Geology and Geophysics 0, 578–588. doi:10.1080/00288306.2020.1781666.

Smith, B., Fricker, H.A., Gardner, A.S., Medley, B., Nilsson, J., Paolo, F.S., Holschuh, N., Adusumilli, S., Brunt, K., Csatho, B., Harbeck, K., Markus, T., Neumann, T., Siegfried, M.R., Zwally, H.J., 2020. Pervasive ice sheet mass loss reflects competing ocean and atmosphere processes. Science 368, 1239–1242. doi:10.1126/science.aaz5845.

Sweeney, D., Kyle, P.R., Oppenheimer, C., 2008. Sulfur dioxide emissions and degassing behavior of Erebus volcano, Antarctica. Journal of Volcanology and Geothermal Research 177, 725–733. doi:10.1016/j.jvolgeores.2008.01.024.

Thomas, I.D., King, M., Bentley, M.J., Whitehouse, P.L., Penna, N.T., Williams, S.D.P., Riva, R.E.M., a. Lavallee, D., Clarke, P.J., King, E.C., a. Hindmarsh, R.C., Koivula, H., 2011. Widespread low rates of Antarctic glacial isostatic adjustment revealed by GPS observations. Geophysical Research Letters 38. doi:10.1029/2011GL049277.

Tréhu, A., Behrendt, J.C., Fritsch, J., 1993. Generalized Crustal Structure of the Central Basin, Ross Sea, Antarctica. Geologisches Jahrbuch Reihe E E 47, 291–311.

Vergniolle, S., Métrich, N., 2021. Open-vent volcanoes: A preface to the special issue. Bulletin of Volcanology 83, 1–5. doi:10.1007/s00445-021-01454-3.

Virtanen, P., Gommers, R., Oliphant, T.E., Haberland, M., Reddy, T., Cournapeau, D., Burovski, E., Peterson, P., Weckesser, W., Bright, J., van der Walt, S.J., Brett, M., Wilson, J., Millman, K.J., Mayorov, N., Nelson, A.R.J., Jones, E., Kern, R., Larson, E., Carey, C.J., Polat, \., Feng, Y., Moore, E.W., VanderPlas, J., Laxalde, D., Perktold, J., Cimrman, R., Henriksen, I., Quintero, E.A., Harris, C.R., Archibald, A.M., Ribeiro, A.H., Pedregosa, F., van Mulbregt, P., SciPy 1.0 Contributors, 2020. {SciPy} 1.0: Fundamental Algorithms for Scientific Computing in Python. Nature Methods 17, 261–272. doi:10.1038/s41592-019-0686-2.

Whitehouse, P.L., Gomez, N., King, M.A., Wiens, D.A., 2019. Solid Earth change and the evolution of the Antarctic Ice Sheet. Nature Communications 10, 1–14. doi:10.1038/s41467-018-08068-y.

Williams, S.D.P., 2008. CATS: GPS coordinate time series analysis software. GPS Solutions 12, 147–153. doi:10.1007/s10291-007-0086-4.

Willis, M.J., 2008. Crustal Motion in the Antarctic Interior from a Decade of Global Positioning System Measurements. Ph.D. thesis. Ohio State University.

Wright, R., 2016. MODVOLC: 14 years of autonomous observations of effusive volcanism from space. Geological Society, London, Special Publications 426, 23–53. doi:10.1144/SP426.12.

Yang, X.M., Davis, P.M., Dieterich, J.H., 1988. Deformation from Inflation of a Dipping Finite Prolate Spheriod in an Elastic Half-Space as a Model for Volcanic Stressing. Journal of Geophysical Research 93, 4257–4549.

Zandomeneghi, D., Aster, R., Kyle, P., Barclay, a., Chaput, J., Knox, H., 2013. Internal structure of Erebus volcano, Antarctica imaged by high-resolution active-source seismic tomography and coda interferometry. Journal of Geophysical Research: Solid Earth 118, 1067–1078. doi:10.1002/jgrb.50073.

Zandomeneghi, D., Kyle, P., Miller, P., Snelson, C., Aster, R., 2010. Seismic tomography of erebus volcano, Antarctica. Eos 91, 53–55. doi:10.1029/2010EO060002.

Zumberge, J.F., Heflin, M.B., Jefferson, D.C., Watkins, M.M., Webb, F.H., 1997. Precise point positioning for the efficient and robust analysis of GPS data from large networks. Journal of Geophysical Research: Solid Earth 102, 5005–5017. doi:10.1029/96JB03860.